ARTICLES
https://doi.org/10.1038/s41593-018-0227-9
nature neuroscience

CNS lymphatic drainage and neuroinflammation are regulated by meningeal lymphatic vasculature

Antoine Louveau[1,2,9*], Jasmin Herz[1,2,9], Maria Nordheim Alme[1,2,3,4], Andrea Francesca Salvador[1,2,5], Michael Q. Dong[1,2], Kenneth E. Viar[1,2], S. Grace Herod[1,2], James Knopp[1,2], Joshua C. Setliff[1,2], Alexander L. Lupi[1,2], Sandro Da Mesquita[1,2], Elizabeth L. Frost[1,2], Alban Gaultier[1,2], Tajie H. Harris[1,2], Rui Cao[6], Song Hu[6], John R. Lukens[1,2], Igor Smirnov[1,2], Christopher C. Overall[1,2], Guillermo Oliver[7] and Jonathan Kipnis[1,2,5,8*]

Neuroinflammatory diseases, such as multiple sclerosis, are characterized by invasion of the brain by autoreactive T cells. The mechanism for how T cells acquire their encephalitogenic phenotype and trigger disease remains, however, unclear. The existence of lymphatic vessels in the meninges indicates a relevant link between the CNS and peripheral immune system, perhaps affecting autoimmunity. Here we demonstrate that meningeal lymphatics fulfill two critical criteria: they assist in the drainage of cerebrospinal fluid components and enable immune cells to enter draining lymph nodes in a CCR7-dependent manner. Unlike other tissues, meningeal lymphatic endothelial cells do not undergo expansion during inflammation, and they express a unique transcriptional signature. Notably, the ablation of meningeal lymphatics diminishes pathology and reduces the inflammatory response of brain-reactive T cells during an animal model of multiple sclerosis. Our findings demonstrate that meningeal lymphatics govern inflammatory processes and immune surveillance of the CNS and pose a valuable target for therapeutic intervention.

One of the principal phenomena arguing in favor of the brain's immune privilege is the apparent lack of lymphatic drainage from the brain parenchyma. This was, however, disputed by experimental evidence showing that tracers and proteins injected into the brain parenchyma and/or the cerebrospinal fluid (CSF) found their way to the brain's peripheral lymph nodes[1–3]. Intraparenchymal macromolecules were shown to exit the parenchyma mainly via perivascular efflux into the CSF[4], while the CSF itself was reported to exit the CNS mainly through arachnoid granulations into the venous system[5] and along the neural sheaths of cranial (particularly the olfactory) nerves, using the perineural lymphatics[2,3,6].

Although immune cells (with the exception of microglia) have no access to the brain parenchyma under homeostatic conditions, the meninges surrounding the brain are populated by a variety of immune-cell types, which not only provide immune surveillance but also affect brain function[7]. The recent demonstration of the presence of functional lymphatic vessels in the brain meninges[1,8] raised the possibility of another drainage path for CSF-contained macromolecules and immune cells directly into the cervical lymph nodes (CLNs). The exact route(s) taken by macromolecules and immune cells to exit the CNS, as well as the contribution of each route to the CNS-associated initiation of immune responses, are still a matter of debate[9,10]. It is important to identify and characterize the route(s) responsible for drainage of CNS-derived antigens because modulation of these may offer a valuable approach to the treatment of CNS-associated neuroinflammatory conditions.

Here we demonstrate that meningeal lymphatic vessels represent an important drainage route for CNS- and CSF-derived soluble molecules and for meningeal immune cells. Meningeal lymphatic endothelial cell transcriptome data suggest the unique biology of these cells, compared to lymphatic endothelial cells from other tissues. Lastly, we show that in mice with experimental autoimmune encephalomyelitis (EAE, an animal model of multiple sclerosis), decreasing the lymphatic drainage under neuroinflammatory conditions leads to diminished acquisition of encephalitogenic properties by antigen-specific T cells, with resulting amelioration of clinical symptoms of EAE.

Results

Access of the cerebrospinal fluid to meningeal lymphatic vessels. To examine whether macromolecules from the CSF can directly access meningeal lymphatics, Prox1^{GFP} reporter mice were injected with a red fluorescent tracer, Qdot^{655}, in the intracisterna magna (i.c.m.), and the fluorescent tracer was followed within meningeal lymphatics using multiphoton intravital imaging (Fig. 1a, b). One hour after Qdot^{655} injection, tracer was detected within the meningeal lymphatic vessels adjacent to the transverse sinus (Fig. 1c). This observation suggests that while meningeal lymphatic vessels

[1]Center for Brain Immunology and Glia (BIG), University of Virginia, Charlottesville, VA, USA. [2]Department of Neuroscience, University of Virginia, Charlottesville, VA, USA. [3]Department of Clinical Medicine, University of Bergen, Bergen, Norway. [4]Department of Neurology, Haukeland University Hospital, Bergen, Norway. [5]Neuroscience Graduate Program, University of Virginia, Charlottesville, VA, USA. [6]Department of Biomedical Engineering, University of Virginia, Charlottesville, VA, USA. [7]Northwestern University, Feinberg School of Medicine, Chicago, IL, USA. [8]Gutenberg Research Fellowship Group of Neuroimmunology, Focus Program Translational Neuroscience (FTN) and Immunotherapy (FZI), Rhine Main Neuroscience Network (rmn^2), University Medical Center of the Johannes Gutenberg University Mainz, Mainz, Germany. [9]These authors contributed equally: Antoine Louveau, Jasmin Herz. *e-mail: al2hk@virginia.edu; kipnis@virginia.edu

are located in the dura matter of the meninges[8,11,12], they have direct access to the CSF. To investigate the potential entry routes of the CSF into the meningeal lymphatics, fluorescently labeled Lyve-1 antibodies were injected into the CSF and followed through meningeal lymphatics at different timepoints. Analysis of whole-mount meninges revealed a time-dependent enhancement of immunostaining of the meningeal lymphatic vessels by the i.c.m.-injected antibody (Fig. 1d, e). Within 5–15 min after injection, specific areas of the lymphatics along the transverse sinus and the meninges covering the olfactory bulb were labeled with the antibody, suggesting that these areas are the first to have contact with CSF (we term these areas 'hot spots'). At later timepoints, larger areas of meningeal lymphatics were covered by Lyve-1 antibodies. The lymphatic appearance of Lyve-1 antibodies was independent of their speed of injection (Supplementary Fig. 1a). Notably, lymphatics along the middle meningeal artery did not appear to be labeled by the injected antibodies (Fig. 1d and Supplementary Fig. 1a), suggesting that these vessels may be draining the dura but not the CSF. Fluorescent proteins, particles (Fig. 1f), or immune cells (Fig. 1g), accumulated at the same areas along the lymphatic vessels after i.c.m. injection. Exogenously labeled T cells injected i.c.m. accumulated mainly around and inside the meningeal lymphatics of the transverse sinus (Fig. 1h). Accumulation of fluorescent microparticles was independent of the route of CSF administration, as cisterna magna and lateral ventricle injections resulted in similar accumulations at the hot spots (Supplementary Fig. 1b). Intranasal injection of fluorescent particles led to only a limited appearance of beads in the meningeal spaces, likely because of the large size of the particles used (Supplementary Fig. 1b).

The intradural localization of the meningeal lymphatic vessels, and the uptake of intravenously injected gadolinium in human and primate meningeal lymphatics[8,12], suggest that meningeal lymphatic vessels are draining the dura matter. Therefore, if the tracer injection results in dural leakage, our interpretation may be incorrect. To address the potential caveat of dural leakage, we injected fluorescent ovalbumin into the cisterna magna of wild-type mice or applied the same amount of ovalbumin to nonfixed dissected skullcaps for 1 h before fixation (Supplementary Fig. 1c,d). Application of fluorescent ovalbumin onto meningeal explants resulted in an uptake of ovalbumin by the meningeal macrophages (most likely through pinocytosis[13]) throughout the entire meninges (Supplementary Fig. 1c,d). However, i.c.m. injection of ovalbumin resulted in its uptake only by macrophages along the sinuses (Supplementary Fig. 1c,d), suggesting that other dural macrophages were not exposed to the ovalbumin injected i.c.m. in vivo. To further substantiate this point, we performed multiphoton imaging of the subarachnoid space above the cerebellum of CX3CR1^{GFP} mice after i.c.m. injection of Qdot^{655}. Qdot^{655} was present below the dura mater (as visualized through the secondary harmonic and intravenous injection of furamidine, which labels nuclei of the dura matter and blood endothelial cells; Supplementary Video 1). Furthermore, ten minutes after i.c.m. injection, fluorescent ovalbumin was found in perivascular spaces of the pial blood vessels of the cerebellum, the hot spots, and the immediate surroundings of the injection site, but not anywhere else in the dura, demonstrating that the ovalbumin circulated within the subarachnoid spaces but not intradurally (Supplementary Fig. 1e).

Using multiphoton live imaging, we demonstrated that within minutes after i.c.m. injection of Qdot^{655}, lymphatics along the transverse sinus (where we observed the hot spots) were filled with the tracer (Fig. 1i), whereas lymphatics along the superior sagittal sinus (lacking hot spots) remained devoid of the tracer (Fig. 1i). Qdot^{655} uptake by the meningeal lymphatics was more rapid in the region of the transverse sinus associated with lymphatic hot spots than in the regions that did not contain hot spots (Supplementary Video 2). Overall, these observations demonstrated that the meningeal lymphatics can uptake and transport CSF constituents.

Close observation of the lymphatics of the transverse sinuses revealed an increase in lymphatic length and the presence of lymphatic extension-like structures (Fig. 1j and Supplementary Fig. 1f), commonly observed in peripheral lymphatic vasculature[14]. The structures were ~1,800 µm from the pineal gland (Fig. 1k, l), correlating with regions of Lyve-1 antibody accumulation at early timepoints after injection. Meningeal lymphatics at the hot spots appeared as sprouts harboring button-like junctions of VE-cadherin and claudin-5 (Fig. 1j and Supplementary Fig. 1f). Although spatial organization of the tight junction proteins in the meningeal lymphatic sprouts revealed a discontinuous pattern (Supplementary Fig. 1f), it was unique and not identical to what was observed on lymphatic sprouts of the diaphragm (Supplementary Fig. 1f and ref. [14]).

Extensions of the meningeal lymphatics along the transverse sinus and the upper part of the superior sagittal sinus can be observed by multiphoton microscopy and might suggest direct exposure to the CSF (Supplementary Fig. 1g,h and Supplementary Video 3). Similarly to peripheral lymphatics, the meningeal lymphatic extensions might represent the entry points for fluid and

Fig. 1 | Meningeal lymphatic subarachnoid extensions uptake molecules and immune cells from the cerebrospinal fluid. a, General scheme of meningeal lymphatic vascular organization. **b**, Scheme of the experiment presented in **c**. Prox1^{GFP} mice were injected in the cisterna magna (i.c.m.) with 5 µL of Qdot^{655}. The transverse sinus was imaged through a thinned skull. **c**, Representative image of meningeal lymphatics adjacent to the transverse sinus (Prox1^{GFP}, green) filled with the i.c.m.-injected Qdot^{655} (red) 60 min after injection. Inset: coronal view of the lymphatic vessel filled with Qdot^{655}. Scale bar, 65 µm. Representative image of 3 independent animals. **d**, Representative images of the lymphatic vessels co-labeled with i.c.m.-injected Alexa Fluor 488-conjugated anti-Lyve-1 (Lyve-1^{A488}) and exogenously applied eFluor 660-conjugated anti-Lyve-1 (Lyve-1^{eF660}) at different timepoints after i.c.m. injection. Inset: arrows at 5 and 15 min illustrate initial points where the i.c.m.-injected Lyve-1^{A488} labeled meningeal lymphatics. Scale bars, 1,000 µm (top); 250 µm (bottom left); 60 µm (bottom right). **e**, Quantification of the percentage of lymphatic vessels labeled by the i.c.m.-injected antibody and total lymphatic area at different timepoints postinjection (mean ± s.e.m.; $n = 4$ mice per group). **f**, Representative images of OVA^{594} (Alexa Fluor 594-conjugated ovalbumin) and fluorescent bead accumulation along the lymphatics (Lyve-1) are shown. Arrows, lymphatic extensions in the area of microbeads and OVA accumulation. Scale bars, 300 µm (top); 120 µm (bottom). Representative images of 5 independent animals. **g**, Representative images of the accumulation of exogenously injected T cells (CFSE, green) at the extension-rich regions of lymphatic vessels adjacent to the transverse sinuses 12 h after i.c.m. injection. Scale bars, 1,000 µm (right); 200 µm (insets). Representative images of 3 independent animals. **h**, Representative images of exogenously injected T cells (green) within the meningeal lymphatics (white) associated with the transverse sinus (blue). Scale bar, 35 µm. Representative images of 5 independent animals. **i**, Representative images of the lymphatics of the superior sagittal sinus (left) and the transverse sinus (right) with i.c.m.-injected Qdot^{655}. Arrows, subarachnoid space (SAS). Scale bar, 25 µm. Representative images of 2 independent animals. **j**, Representative images of lymphatic sprout at the extension-rich region of lymphatic vessels along the transverse sinus, immunostained with Lyve-1 (gray) and junction proteins VE-cadherin (green) and claudin-5 (red). Scale bar, 25 µm. Representative images of 2 independent animals. **k**, Representative image of the meningeal lymphatic vessels adjacent to the transverse sinus of Prox1^{GFP} mice. Arrows, sprouting or extensions along the lymphatic vessels. Scale bar, 350 µm. Representative image of 5 mice. **l**, Quantification of the lengths and numbers of lymphatic extensions in adjacent sections of meningeal lymphatics associated with the transverse sinus starting from the pineal gland (mean ± s.e.m.; $n = 5$ mice; $n = 2$ transverse sinuses per mouse).

macromolecules into the meningeal lymphatic vasculature from the subarachnoid space and/or CSF.

The network of meningeal lymphatics previously described did not appear to only cover the forebrain but was also present in the spinal cord meninges, more specifically along the nerve roots[15] (Supplementary Fig. 2a–e). The lymphatic extensions were also observed on the cerebellar ring of lymphatics (Supplementary Fig. 2f), suggesting that multiple sites along the meningeal lymphatic network might have access to CSF. Similarly, fluorescent microparticles injected into the CSF through the lateral ventricle or cisterna magna were seen accumulating near the lymphatics of the cervical nerve roots in the spinal cord meninges (Supplementary Fig. 2g).

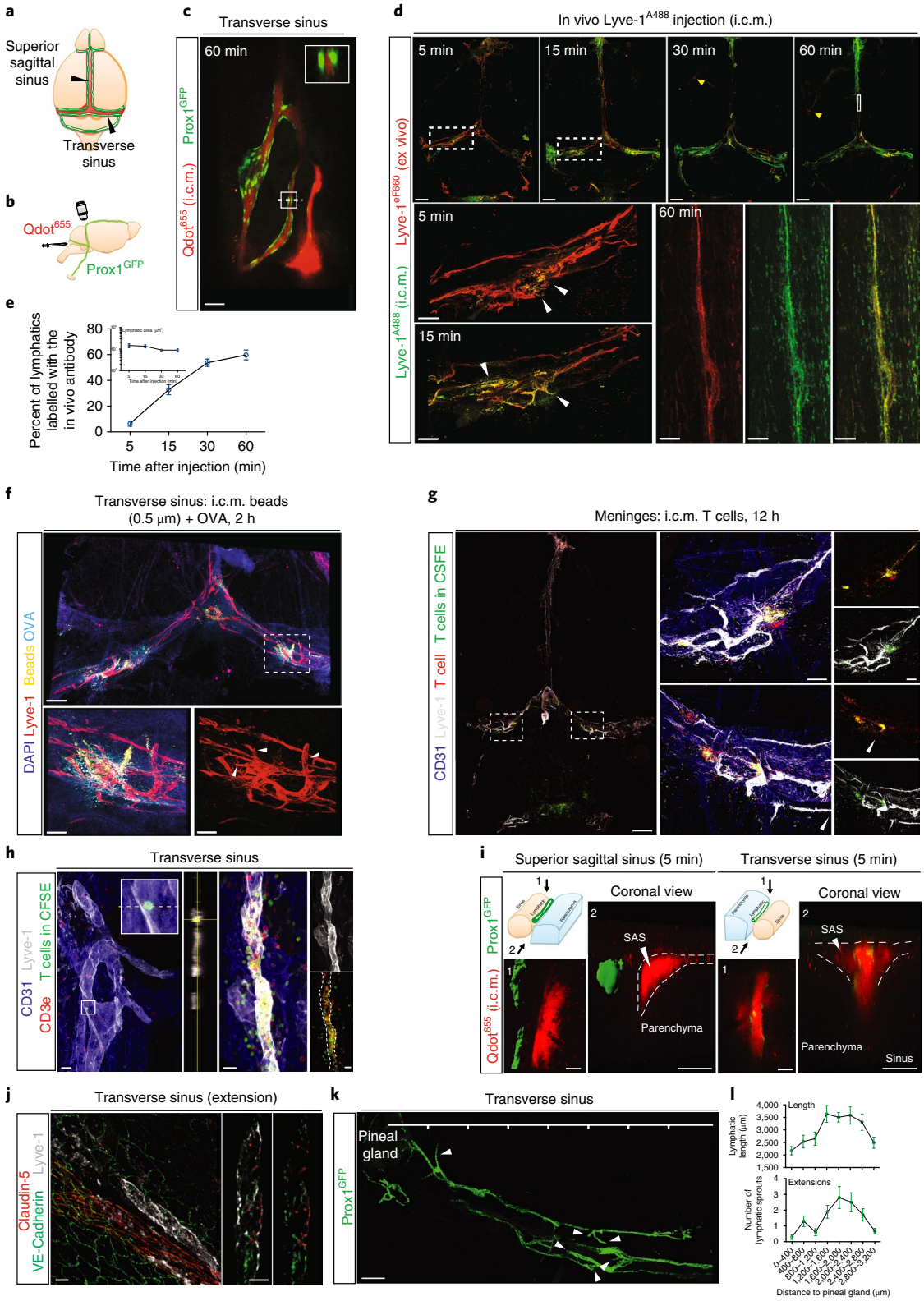

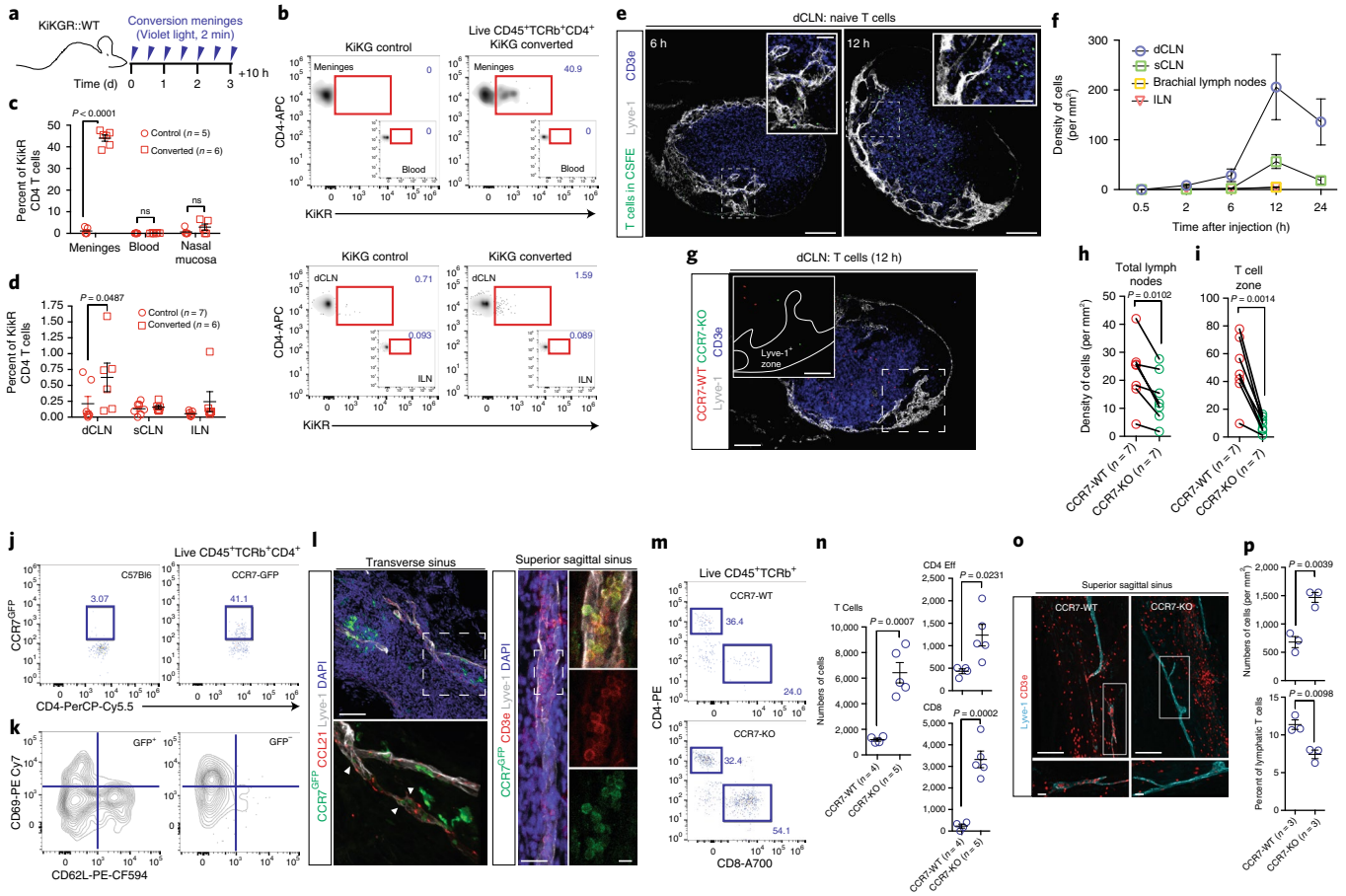

Fig. 2 | Meningeal T cells migrate into the cervical lymph nodes in a CCR7-dependent manner. a, Scheme of the experiments in **b**–**d**. C57Bl6 mice were reconstituted with bone marrow from KiKGR mice after irradiation. Ten weeks after reconstitution, meninges were converted for 2 min with a violet light (through the intact skull) every 12 h for 3 d. Ten hours after the last conversion, tissues were harvested and analyzed by fluorescence-activated cell sorting (FACS). **b**, Representative density plots of converted T cells (KiKR$^+$) in the meninges and dCLN of control and converted mice. APC, allophycocyanin. **c**, Quantification of the percentage of converted CD4 T cells (KiKR$^+$) in the meninges, blood, and nasal mucosa of control and converted mice (mean ± s.e.m.; $F_{1,26} = 388.8$; two-way ANOVA with Sidak's multiple-comparisons test). **d**, Quantification of the percentage of KiKR$^+$ CD4 T cells in the dCLN, sCLN, and inguinal lymph nodes (ILN) of control and converted mice (mean ± s.e.m.; $F_{1,33} = 4.862$; mice pooled from 2 independent experiments, two-way ANOVA with Sidak's multiple-comparisons test). **e**, Representative images of i.c.m.-injected naive T cells in the dCLN of mice at 6 and 12 h postinjection. Scale bar, 200 µm; insets, 50 µm. **f**, Quantification of the density of naive T cells per mm^2 of dCLN, sCLN, brachial lymph nodes, and ILN at different timepoints postinjection (mean ± s.e.m.; $n = 2$–7 mice per group, pooled from 2 independent experiments). **g**, Representative images of CCR7-WT and CCR7-KO CD4 T cells in dCLN 12 h postinjection. Scale bar, 200 µm; inset, 75 µm. **h**,**i**, Quantification of the density of CCR7-WT and CCR7-KO cells per mm^2 of total lymph nodes (**h**) or per T cell zone (**i**) 12 h postinjection (mean ± s.e.m.; (**h**) $t_6 = 3.687$; (**i**) $t_6 = 5.586$; pooled from 2 independent experiments; two-tailed paired *t* test). **j**, Representative dot plots of GFP expression by CD4 T cells in the meninges of C57Bl6 mice and CCR7^{GFP} mice. Representative of 3 mice. **k**, Representative contour plot of phenotype of CCR7$^+$ and CCR7$^-$ CD4 T cells in the meninges of CCR7^{GFP} mice. Representative of 3 mice. **l**, Representative images of CCR7 expression (green) in and around the meningeal lymphatics (Lyve-1 and CCL21) along the transverse and superior sagittal sinuses. Arrows, leukocyte-shaped cells expressing CCR7 inside the meningeal lymphatics. Scale bar, 120 µm. CCR7-expressing T cells (CD3e, red) are found in the meningeal lymphatics (Lyve-1). Scale bar, 40 µm; insets, 15 µm. Representative images of 3 mice. **m**, Representative dot plots of meningeal T cells (CD4 and CD8) in the meninges of adult CCR7-WT and CCR7-KO mice. **n**, Quantification of the number of total, CD4 effector (eff), and CD8 T cells in the meninges of CCR7-WT and CCR7-KO mice (mean ± s.e.m.; representative of 2 independent experiments; $t_7 = 5.744$ (T cells), $t_7 = 2.897$ (CD4 eff), $t_7 = 6.961$ (CD8); two-tailed unpaired *t* test). **o**, Representative images of T cells (CD3e) in and around the meningeal lymphatics (Lyve-1) of the superior sagittal sinus in CCR7-WT and CCR7-KO mice. Scale bar, 120 µm; inset, 15 µm. **p**, Quantification of the density of T cells in the proximity of the sinuses of CCR7-WT and CCR7-KO mice (top) and percentage of T cells localized inside the lymphatics (bottom; mean ± s.e.m.; $t_4 = 5.998$ (density), $t_4 = 4.633$ (percentage); two-tailed unpaired *t* test).

Previous reports describe a lymphatic network at the sides and base of the skull as well as the spinal[8,16,17] (Supplementary Fig. 2h–j). After i.c.m. injection, some of the fluorescent particles are seen accumulating around the sides of the skull, close to lymphatic vessels (Supplementary Fig. 2j). These vessels, however, seemed to have lymphatic valves, as previously described[8], suggesting they were collecting lymphatics, which are usually less accessible by macromolecules. Overall, these results suggest the existence of particular spots along meningeal lymphatic vessels that serve as entry points for solutes and immune cells from the subarachnoid space and CSF.

Trafficking of meningeal T cells to the deep cervical lymph nodes is CCR7-dependent. Given that meningeal spaces are populated by numerous T cells[16], and that those T cells can enter the

meningeal lymphatics (Fig. 1h), we hypothesized that meningeal T cells use lymphatic vessels to reach the CLNs. In Prox1^{GFP}Lck^{tdTOMATO} mice (in which lymphocyte protein tyrosine kinase is primarily expressed by T cells and some NK cells[18]) we observed endogenous lymphocytes inside the lymphatic extensions (Fig. 1h and Supplementary Fig. 3a). Using KiKume Green Red (KiKGR) mice allows photoconversion and in vivo tracing of endogenous cells in a specific anatomical location (from KiKG (green fluorescence) to KiKR (red) in response to violet light exposure). Serial illumination through an intact skull resulted in 40 to 45% conversion of meningeal and CSF KiKG$^+$ CD4 T cells into KiKR$^+$ T cells (Fig. 2a–c) without targeting the blood-circulating CD4 T cells (Fig. 2c). Analysis of brain-draining deep and superficial CLNs (dCLNs and sCLNs, respectively), as well as nonbrain draining inguinal lymph nodes, after serial conversion of the meningeal spaces revealed an accumulation of KiKR$^+$ CD4 T cells uniquely in the dCLN of the converted mice (Fig. 2b, d). While the conversion was limited to the meningeal regions accessible by the laser, these results demonstrate that T cells, localized in the meningeal and CSF spaces (subarachnoid spaces, pia, CSF, and dura), trafficked to dCLNs under physiological conditions. Naive CD4 T cells injected into the CSF of naive adult mice accumulated primarily in the dCLNs and sCLNs (Fig. 2e, f). T cell accumulation in the dCLNs was first observed in the lymph vessels of the lymph nodes and subsequently in the T cell zone (Fig. 2e). Using flow cytometry, we showed that similar numbers of i.c.m. injected T cells drained into dCLNs and sCLNs, but that the percentage of GFP$^+$ T cells was higher in the dCLNs than the sCLNs (Supplementary Fig. 3b–d). These results confirm previous reports[2,3,6] on dCLNs and sCLNs being the major CNS-draining lymph nodes.

Because meninges are mainly populated by central memory T cells[19], we injected in vitro-generated central memory CD4 T cells (Supplementary Fig. 3e) into adult mice and found them accumulating in the dCLNs (Supplementary Fig. 3f,g). Co-injection of naive and central memory CD4 T cells showed that efficiency of drainage was similar between the two cell types (Supplementary Fig. 3h).

Migration of immune cells requires attraction through a chemokine gradient, along with the expression of integrins and other adhesion molecules. Most of these signals involve the activation of G-protein-coupled receptors[20]. Pretreatment of CD4 T cells with the G-protein-coupled receptor inhibitor pertussis toxin resulted in their failure to drain into the dCLNs as efficiently as control CD4 T cells (Supplementary Fig. 3i,j).

The CCR7–CCL21 pathway has been described as the main pathway for T cells and dendritic cells (DC) to circulate through the lymphatic system, and it mediates both entry and intralymphatic migration of cells under both physiological and pathological conditions[21,22] (although additional pathways contribute to immune cell trafficking under inflammatory conditions[23]). To address the role of CCR7 in meningeal cell trafficking, we co-injected wild-type CCR7 (CCR7-WT) and CCR7-knockout (CCR7-KO) T cells at a 1:1 ratio into the CSF of naive mice. Drainage of CCR7-KO T cells in the dCLNs was significantly reduced compared to that of CCR7-WT T cells (Fig. 2g–i). Similarly to T cells, injection of in vitro-generated DCs (Supplementary Fig. 3k,l) led to their entry into the meningeal lymphatic around the hot spots (Supplementary Fig. 3m). Using the KiKGR system, we demonstrated that endogenous DCs migrated from the meninges to the dCLNs after mobilization with polyinosinic:polycytidylic acid (Poly(I:C)) (Supplementary Fig. 3n–r). Their migration into the dCLNs (Supplementary Fig. 3s,t)

Fig. 3 | Meningeal lymphatics as the main route for immune cell and macromolecule drainage from the CSF. a, Representative images of exogenously injected T cells (CellTracker Deep Red Dye, red) in dCLN 12 h after i.c.m. injection in sham-operated (sham) or ligated mice (24 h postsurgery). Scale bar, 150 µm. **b**, Quantification of the density of T cells per mm^2 of dCLN and sCLN in sham-operated or ligated mice (mean ± s.e.m.; $F_{1,14} = 7.676$; two-way ANOVA with Sidak's multiple-comparison test). **c**, Representative images of exogenously injected fluorescent microbeads (0.5 µm in diameter; green) in the dCLN of sham-operated or ligated mice. Scale bar, 150 µm. **d**, Quantification of the percentage of bead coverage in the dCLN of sham-operated or ligated mice (5 µL of beads were injected); expressed as percentage of the control condition (mean ± s.e.m.; $t_8 = 4.603$; two-tailed unpaired *t* test). **e**, Quantification of the size of the dCLNs of sham-operated or ligated mice (mean ± s.e.m.). **f**, Representative contour plots of T cells in the meninges of sham-operated or ligated mice. Quantification of the number of T cells (TCRb$^+$) in the meninges sham-operated or ligated mice (mean ± s.e.m.; representative of 2 independent experiments; $t_8 = 3.813$; two-tailed unpaired *t* test). **g**, Representative images of i.c.m.-injected T cells (Deep Red Cell Tracker, red) in the lymphatics of the cribriform plate (i) and in and around the lymphatics at the base of the nose (ii,iii). White arrowheads, intralymphatic T cells; yellow arrowheads, perilymphatic T cells. Scale bar, 1,000 µm; insets, 50 µm. Representative images of 2 independent mice. **h**, Representative images of the cribriform plate region 12 h after i.c.m. injection of CFSE-labeled T cells (green). Arrowhead points to a CFSE-labeled T cell on the nasal side of the cribriform plate. Scale bar, 230 µm. Representative images of 4 independent mice. **i**, Quantification of the number of exogenously injected T cells in the meninges (gray), in the meningeal lymphatics (orange), and in the nasal mucosa (green) of mice at different timepoints after i.c.m. injection (mean ± s.e.m.; $n = 2$–8 mice per group, pooled from 2 independent experiments). **j**, Representative images of the meningeal lymphatics (Lyve-1) and blood (CD31) vasculature of mice treated with laser alone, Visudyne (i.c.m.) alone, and Visudyne (i.c.m.) + laser 4 d after photoconversion. Scale bar, 1,000 µm; insets, 400 µm. **k**,**l**, Quantification of the Lyve-1 (**k**) and CD31 (**l**) coverage on the superior sagittal and transverse sinuses of mice treated with laser alone, Visudyne (i.c.m.) alone, and Visudyne (i.c.m.) + laser 4 d after photoconversion (mean ± s.e.m.; representative of 3 independent experiments; $F_{2,18} = 10.67$; two-way ANOVA with Sidak's multiple-comparisons test). **m**, Representative images of the nasal lymphatics (Prox1^{GFP} and Lyve1) 24 h after laser or intranasal (i.n.) injection of Visudyne. Inset: the lymphatic bundle at the base of the skull is ablated after Visudyne treatment. Scale bar, 500 µm; insets, 200 µm. Representative images of 6 mice per group from 2 independent experiments. **n**,**o**, Representative images of i.c.m.-injected T cells (CFSE-labeled) in the dCLNs (**n**) or sCLNs (**o**) of mice treated with laser alone, Visudyne alone, Visudyne i.c.m. + laser, and Visudyne (i.n.) + laser 12 h after i.c.m. injection. Scale bars, (**n**) 150 µm; insets, 30 µm; (**o**) 300 µm; insets, 50 µm. **p**, Quantification of the density of T cells per mm^2 of dCLNs (left) and size of dCLNs (right) in mice treated with laser alone, Visudyne alone, Visudyne i.c.m. + laser, and Visudyne (i.n.) + laser 12 h after i.c.m. injection (mean ± s.e.m.; pooled from 4 independent experiments (left); pooled from 3 independent experiments (right); Kruskal–Wallis test with Dunn's multiple-comparisons test). **q**, Quantification of the density of T cells per mm^2 of sCLNs (left) and sCLN size (right) in mice treated with laser alone, Visudyne alone, Visudyne i.c.m. + laser, and Visudyne (i.n.) + laser 12 h after i.c.m. injection (mean ± s.e.m.; pooled from 2 independent experiments (left) and from a single experiment (right); $F_{3,49} = 4.282$; one-way ANOVA with Sidak's multiple-comparisons test). **r**, Representative images of CSF-injected beads drained to the dCLNs in mice treated with Visudyne (i.n.) + laser and Visudyne (i.c.m.) + laser 2 h after injection. Scale bar, 150 µm; insets, 35 µm. **s**, Quantification of the percentage of bead coverage of the dCLNs of mice treated with laser, Visudyne (i.c.m.) + laser, and Visudyne (i.n.) + laser 2 h after CSF injection (mean ± s.e.m.; $F_{2,23} = 9.122$; one-way ANOVA with Tukey's multiple-comparisons test). **t**, Scheme of the proposed model of the route of drainage into the cervical lymph nodes. **u**, Left: representative contour plots of T cells in the meninges of mice treated with laser and Visudyne (i.c.m.) + laser 7 d postablation. Right: quantification of the numbers of T cells in the meninges of mice treated with laser and Visudyne (i.c.m.) + laser (mean ± s.e.m.; pooled from 3 independent experiments; $t_{23} = 3.939$; two-tailed unpaired *t* test).

was CCR7-dependent, as CCR7-deficient DCs failed to drain to dCLNs from CSF (Supplementary Fig. 3u,v)[24].

Fluorescence-activated cell sorting analysis of meningeal T cells in mice expressing GFP under the CCR7 promoter demonstrated that about 40% of the meningeal CD4 T cells expressed CCR7 (Fig. 2j) and were CD69$^-$CD62L$^{-/intermediate}$, suggesting a recirculating phenotype (Fig. 2k). Immunostaining of the meninges from CCR7^{GFP} mice revealed CCR7$^+$ T cells primarily in close relationship with CCL21$^+$ lymphatic endothelial cells (Fig. 2l). CCR7-KO mice showed increased numbers of meningeal T cells (Fig. 2m–p) and partial exclusion of the meningeal T cells from the lymphatic compartment (Fig. 2o, p).

Meningeal lymphatic vessels serve as a route for drainage of immune cells and macromolecules from CSF. To demonstrate that T cell egress and macromolecule drainage is dependent on the lymphatic vasculature, we first analyzed meningeal drainage in mice heterozygous for the transcription factor prospero homeobox

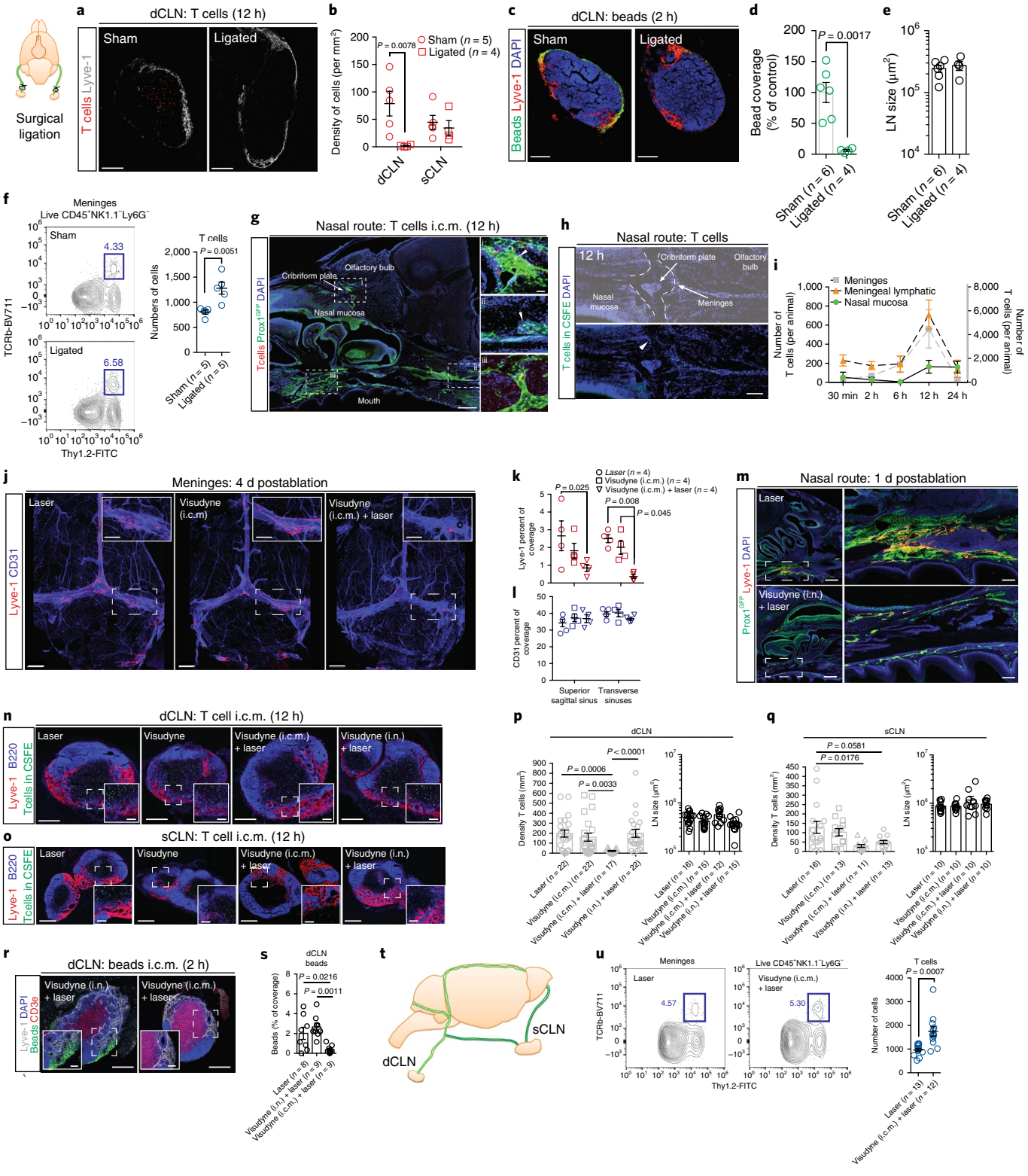

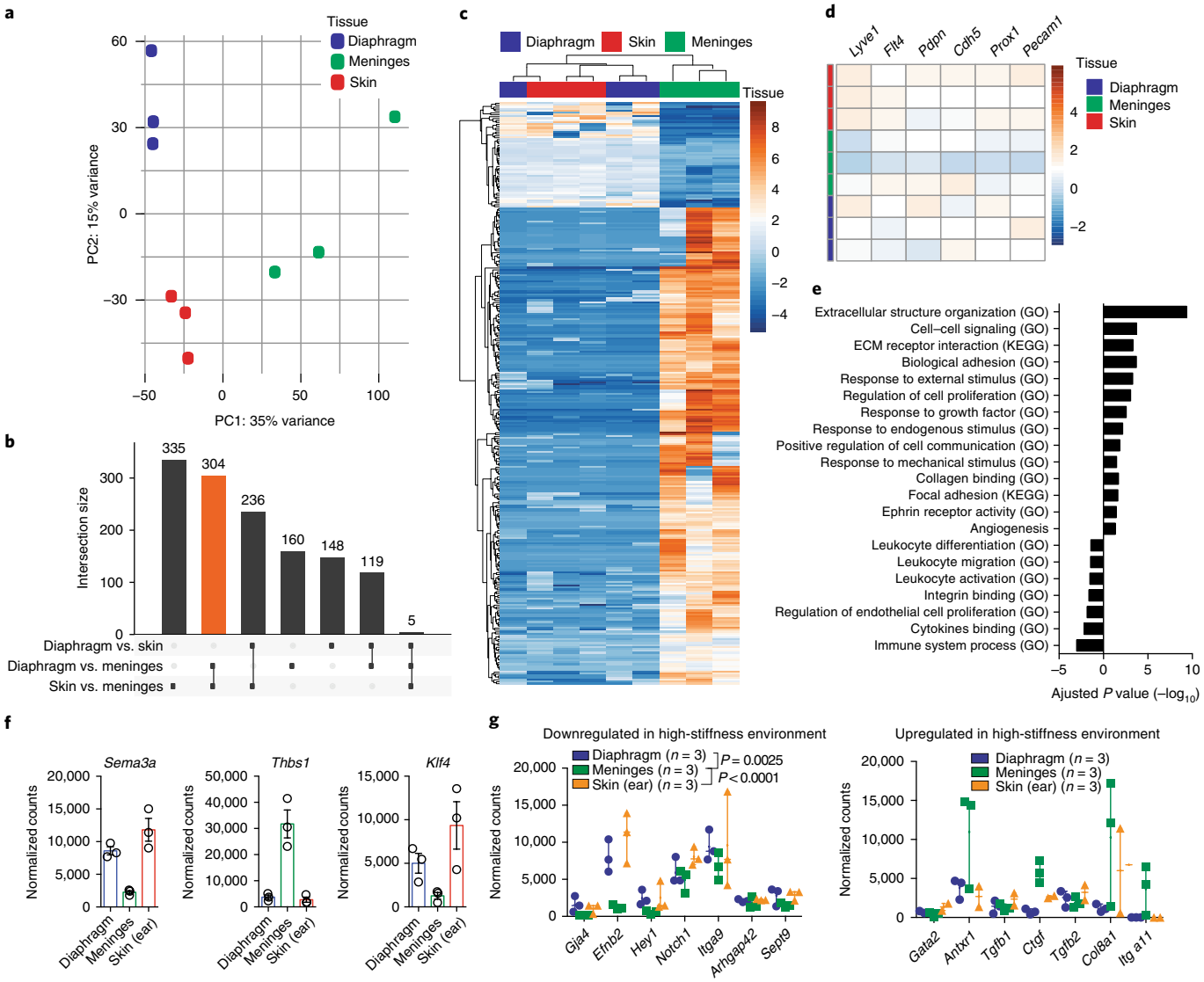

Fig. 4 | Transcriptomic analysis of the meningeal lymphatic endothelial cells. a, Principal component (PC) analysis of the transcriptome of LECs of the diaphragm, meninges, and skin (from the ear; $n = 3$ biological replicates per group, each pooled from 10 individual mice). **b**, UpSet plot showing the set intersections between differentially upregulated genes in meningeal, diaphragm, and skin LECs. The orange bar represents the 304 upregulated genes in the meningeal LEC compared to the diaphragm and skin LEC. Each dot is a visual indicator of the genes comparison. When connected, the bar represents the intersection of genes in common between the two (or more) comparisons. **c**, Heat map of significantly up- and downregulated genes in the meningeal LEC compared to the diaphragm and skin LEC. The color scale is the rlog-transformed values across samples ($P < 0.05$, Fisher's exact test). **d**, Heat map of the relative expression of the LEC-related genes in the meningeal, diaphragm, and skin LEC. The color scale is the rlog-transformed values across samples. **e**, Representation of significantly up- and downregulated gene pathways in the meningeal LEC compared to diaphragm and skin LEC (Fisher's exact test). GO, gene ontology; KEGG, Kyoto Encyclopedia of Genes and Genomes. **f**, Quantification of the normalized counts for *Sema3a*, *Ephb2*, *Thsp1*, and *Klf4* in diaphragm, meningeal, and skin LECs. Genes were selected from the significantly up- or downregulated genes (mean ± s.e.m.). **g**, Quantification of the normalized counts from diaphragm, meninges, and skin LECs for genes previously shown to be down- or upregulated by LECs when cultured on high-stiffness surfaces (mean ± s.e.m.; $F_{2,42} = 12.14$; two-way ANOVA with Tukey's multiple-comparisons test).

protein 1 (Prox1), the master regulator of lymphatic endothelial cell (LEC) fates[25]. Homozygous mice are embryonically lethal, whereas heterozygous (het) mice survive to adulthood, although their lymphatic compartment is mispatterned and leaky[26]. Prox1 has been shown to be expressed by neurons, but Prox1 heterozygote neurons do not appear to be affected[27]. We found that T cells (Supplementary Fig. 4a,b) and macromolecules (Supplementary Fig. 4c,d) injected into the CSF of two month old Prox1^{het} mice failed to drain as efficiently into the dCLNs as in WT littermates (no difference in lymph node size was observed; Supplementary Fig. 4e). Notably, the number of endogenous meningeal T cells was significantly higher in Prox1^{het} ($P = 0.0034$) mice compared to WT littermates (Supplementary Fig. 4f,g). These results suggest that drainage from the meninges was dependent on lymphatic vascular integrity. Because Prox1^{het} mice present a global defect in lymphatic vasculature, we surgically ligated afferent lymphatics reaching the dCLNs, a procedure previously shown to impair drainage of Evans blue from CSF to dCLNs[1]. Similarly to Prox1^{het} mice, T cells (Fig. 3a, b), dendritic cells (Supplementary Fig. 4h,i), and fluorescent microbeads (Fig. 3c, d) injected into the CSF of ligated mice failed to drain into

the dCLNs. The ligation procedure did not affect the lymph node size (Fig. 3e). Notably, the drainage of T cells into the sCLNs was unaffected by the surgical ligation (Fig. 3b), suggesting that meningeal efferent lymphatics might split at some point along its path to enter sCLNs and dCLNs. Endogenous meningeal T cell numbers were increased in the meninges after the ligation of dCLNs afferent lymphatics (Fig. 3f), further strengthening the connection between lymphatic drainage and meningeal T cell compartment.

Previous works have suggested the cribriform plate and nasal mucosa lymphatics as a route for immune cells to exit the CNS and reach the cervical lymph nodes[2]. Indeed, the cribriform plate and nasal mucosa harbored an organized lymphatic vasculature expressing all hallmarks of lymphatic endothelial cells (Supplementary Fig. 4j–o). Staining for endogenous T cells usually did not detect T cells on the nasal side of the cribriform plate (Supplementary Fig. 4p,q), and no KiKR^{+} CD4 T cells were found in the nasal mucosa upon conversion of the meningeal T cells (Fig. 2c). T cells injected i.c.m. were found on the CNS side of the cribriform plate closely associated with or inside the lymphatic network (Fig. 3g–i), with increasing abundance relative to the speed of injection (Supplementary Fig. 4r,s).

To assess whether this experimental model reflects a physiological trafficking pattern of meningeal T cells, we exploited a variety of techniques to directly and specifically ablate meningeal lymphatics. First, we crossed Prox1^{creERT2} mice with either diphteria toxin receptor (DTR)$^{loxP/loxP}$ or diphteria toxin A (DTA)$^{loxP/loxP}$ mice and administered 4-hydroxytamoxifen or diphtheria toxin i.c.m. Unfortunately, both systems resulted in lethality, even in control mice that did not harbor either the DTR or DTA transgene or failure to induce recombination at lower dose (Supplementary Fig. 4t–x). This limitation led us to use a pharmacochemical approach to ablate meningeal lymphatic vessels. Visudyne, a photoconvertible compound that produces short-lived reactive oxygen species upon conversion with a nonthermal 689-nm laser, has been shown to efficiently ablate peripheral lymphatic vessels[28]. We injected Visudyne into the cisterna magna of WT mice, and after 15–30 min (to enable the compound to accumulate in the lymphatics), the laser was applied through the intact skull at five different spots located above the transverse and superior sagittal sinuses, as well as above the lymphatic ring posterior to the cerebellum. This treatment resulted in efficient and stable elimination of the meningeal lymphatic vasculature (Fig. 3j, k and Supplementary Fig. 5a,b).

No difference in intracranial pressure was observed between laser alone (mice were injected with phosphate-buffered saline, PBS), Visudyne (i.c.m.) + laser, or Visudyne (i.cm.) + laser mouse groups at 3 d after ablation (Supplementary Fig. 5c,d). Visudyne treatment also did not alter vascular integrity and function (Fig. 3l and Supplementary Fig. 5e–j) nor did we observe alteration in the integrity of the pia or glia limitans (Supplementary Fig. 5k,l). CSF cytokines and chemokines were slightly upregulated 1 d postinjection in Visudyne-treated mice, as compared to PBS-injected controls, but by day 4 no difference between the PBS and Visudyne treated groups was observed (Supplementary Fig. 5m,n). Moreover, neither proliferation nor activation of meningeal macrophages (Supplementary Fig. 5o–q,t–w) and recruitment of innate immune cells (Supplementary Fig. 5t,u) was evident. Activation of the brain and spinal cord vasculature after Visudyne treatment appeared to be mildly increased, as indicated by modest upregulation of ICAM1 on day 1 after treatment, levels of which were reversed to control baseline after 4 days (Supplementary Fig. 5r,s).

To address the contribution of the nasal route to CNS drainage, we designed a similar approach to ablate nasal lymphatics. Visudyne was injected intranasally and the laser was aimed through the mouth at the base of the nasal cavity. This treatment resulted in the ablation of the lymphatic bundle located at the base of the nose (Fig. 3m). Fluorescently labeled T cells were injected into the CSF of mice with ablated meningeal lymphatics (Visudyne (i.c.m.) + laser), ablated nasal lymphatics (intranasal Visudyne + laser), or two different control groups (PBS (i.c.m.) + laser or Visudyne (i.c.m.) without laser), 4 d after the treatment. Ablation of the meningeal

Fig. 5 | Ablation of lymphatic drainage modulates T cell activation and ameliorates disease development. a, EAE clinical symptoms development in mice treated with laser, Visudyne (i.n.) + laser, and Visudyne (i.c.m.) + laser on the day of EAE induction (mean ± s.e.m.; pooled from 3 independent experiments; $F_{2,79} = 23.07$; repeated measures two-way ANOVA with Tukey's multiple-comparisons test). MOG, myelin oligodendrocyte glycoprotein; CFA, complete Freund adjuvant. **b**, Incidence of EAE development (the day mice reach a score of ≥ 1) in mice treated with laser, Visudyne (i.n.) + laser, and Visudyne (i.c.m.) + laser (pooled from 3 independent experiments, Mantel–Cox log-rank test). **c**, Representative dot plots of CD4 and CD8 T cells in the spinal cord, brain meninges, and spinal cord meninges of mice treated with laser and Visudyne (i.c.m.) + laser during late-onset EAE (day 17). APC, allophycocyanin. **d**, Quantifications of numbers of CD4 and CD8 T cells in the spinal cord, brain meninges, and spinal cord meninges of mice treated with laser and Visudyne (i.c.m.) + laser at day 17 postimmunization (mean ± s.e.m.; pooled from 2 independent experiments; $F_{1,26} = 5.5990$, brain meninges; $F_{1,26} = 10.91$; two-way ANOVA with Sidak's multiple-comparisons test). **e**–**h**, Adult WT mice were injected intravenously (i.v.) with a 1:1 ratio of 2D2^{TdTOMATO} and OTII^{GFP} T cells (4 million cells total). One day after injection, mice were treated with laser or Visudyne (i.c.m.) + laser, and EAE was induced by immunization with MOG_{35-55}. The dCLNs were harvested at day 8 of EAE development and the interaction of the 2D2 and OTII T cells with CD11c^{+} cells were analyzed. (**e**) Representative images of MOG-specific T cells (2D2) and OVA-specific T cells (OTII) in the dCLNs of mice treated with laser and Visudyne (i.c.m.) + laser at day 8 after EAE induction. Green arrowheads, OTII T cells. Yellow arrowheads, 2D2 cells not in contact with CD11c^{+} cells; white arrowheads, 2D2 cells in contact with CD11c^{+} cells. Scale bar, 150 µm; insets, 25 µm. Representative of 5 independent mice per group. (**f**) Representative images and associated profile plots of MOG-specific T cells (2D2, red) in close contact (top) or not in contact (bottom) with CD11c^{+} cells (cyan) in the dCLNs of mice treated with laser and Visudyne (i.c.m.) + laser 8 d after EAE induction. Scale bar, 10 µm. Representative of 5 independent mice per group. (**g**) Quantification of the density of OTII and 2D2 T cells in the dCLNs of mice treated with laser and Visudyne (i.c.m.) + laser 8 d after EAE induction (mean ± s.e.m.). (**h**) Quantification of the percentage of OTII and 2D2 T cells in contact with CD11c^{+} cells in the dCLNs of mice treated with laser and Visudyne (i.c.m.) + laser 8 d after EAE induction (mean ± s.e.m.; $F_{1,8} = 4.204$; two-way ANOVA with Sidak's multiple-comparisons test). **i**, Heat map of the significantly up- and downregulated genes in the CD44^{+} 2D2 T cells obtained from dCLN and spleen of mice treated with Visudyne (i.c.m.) + laser vs. control laser-treated mice (Fisher's exact test with $P > 0.05$). The color scale bar is rlog-transformed values across samples. **j**, Volcano plot of the significantly up- and downregulated genes in the CD44^{+} 2D2 T cells obtained from dCLN of mice treated with Visudyne (i.c.m.) + laser vs. control laser-treated mice ($n = 3$ samples per group; P values ($P_{adj.}$ adjusted P values) were corrected for multiple hypothesis testing with the Benjamini–Hochberg false-discovery rate (FDR) procedure). **k**, Representation of some of the significantly enriched pathways in the CD44^{+} 2D2 T cells obtained from dCLN of mice treated with Visudyne (i.c.m.) + laser vs. control laser-treated mice (P values were corrected for multiple hypothesis testing with the Benjamini–Hochberg FDR procedure). **l**, Dot plot analysis of the active miRNAs in CD44^{+} 2D2 T cells obtained from dCLN of the mice treated with Visudyne (i.c.m.) + laser vs. control laser-treated mice (data analyzed using the hypergeometric distribution with significance at $P < 0.05$). pv, P value based on the total number of differentially expressed (DE) target genes versus the total number of target genes; pvn, P value based on the number of downwardly expressed DE targets versus the total number of DE targets.

lymphatics resulted in a significant decrease of T cell accumulation in both dCLNs and sCLNs (Fig. 3n–q). Ablation of the nasal lymphatic route significantly decreased drainage into the sCLNs, but not into the dCLNs (Fig. 3n–q). Similarly, drainage of beads into the dCLNs was only affected by the disruption of meningeal but not nasal lymphatics (Fig. 3r, s). Notably, lymphatics of the cribriform plate remained intact when meningeal lymphatics were ablated (Supplementary Fig. 5x), and the ability of injected T cells to cross the cribriform plate was also not impacted (Supplementary Fig. 5y). These results may be indicative of meningeal lymphatics draining into both the dCLNs and sCLNs, while the nasal lymphatics may drain primarily into the sCLNs (Fig. 3t). Strikingly, when the laser was aimed at spots outside of the lymphatic vasculature to induce the potential meningeal side effects via reactive oxygen species production without meningeal lymphatic ablation, we found no difference in T cell migration compared to control mice (Supplementary Fig. 5z). Likewise, ablation of the meningeal lymphatics resulted in accumulation of endogenous T cells in the meningeal compartment (Fig. 3u). These results collectively suggest that the meningeal lymphatic vessels are an important route for CSF cellular and molecular constituents to reach the dCLNs, whereas both meningeal and cribriform or nasal routes connect to sCLNs.

RNA-seq of meningeal lymphatic endothelial cells reveals a unique transcriptomic signature. Lymphatic endothelial cells have been shown to proliferate and expand in an inflammatory environment[29]. We used the animal model of multiple sclerosis, EAE, to induce robust inflammation in the CNS, including in the CSF and meningeal spaces[30,31]. Analysis of the meningeal lymphatic vasculature at different timepoints after immunization of mice revealed no morphological changes in both brain and spinal cord meningeal lymphatics (Supplementary Fig. 6a–d). Notably, later in

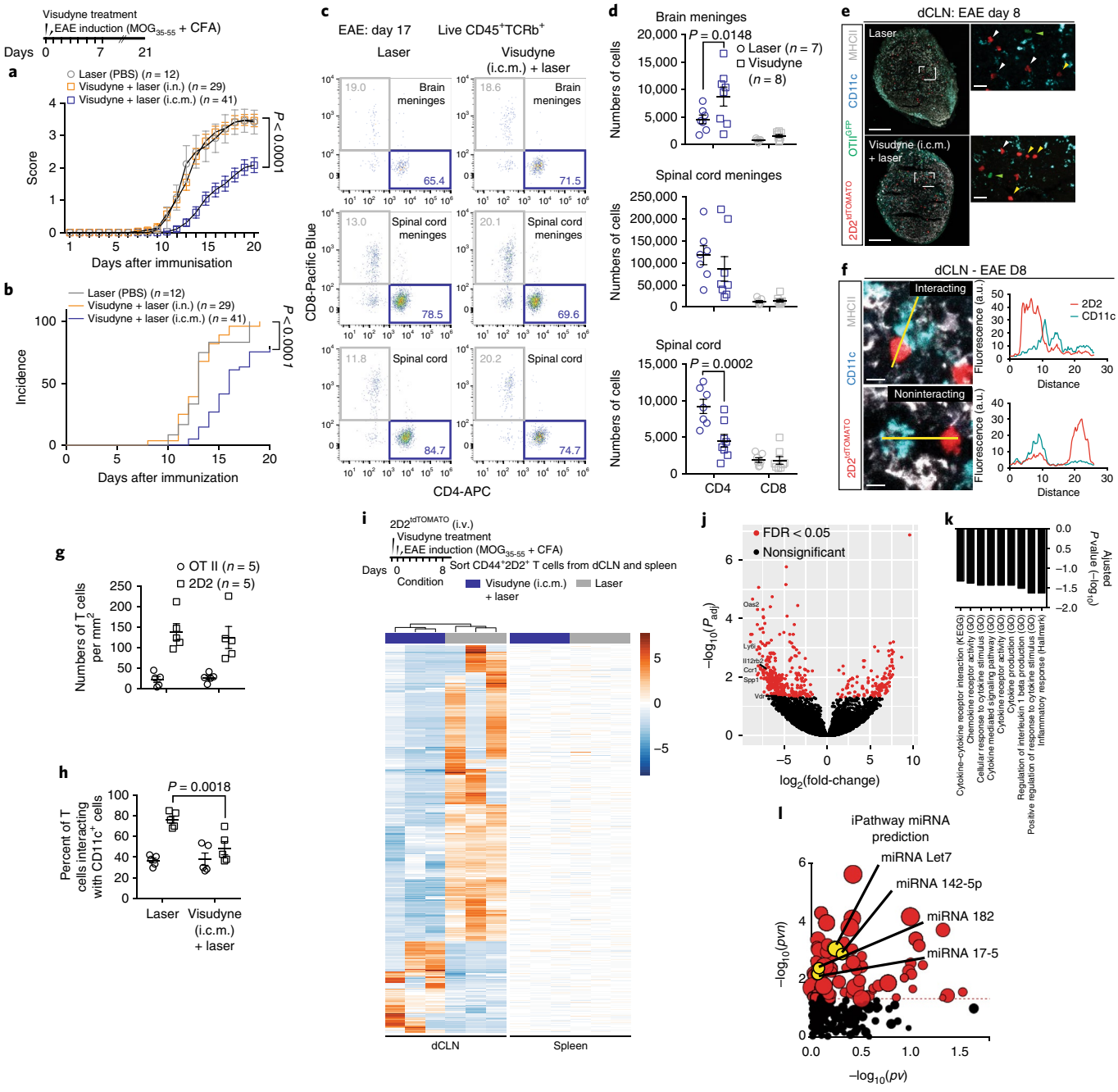

the disease, lymphatics located on the CNS side of the cribriform plate did expand (Supplementary Fig. 6e,f), suggesting potential increased drainage through the nasal route in late stages of the disease. Indeed, VEGFc, among other prolymphangiogenic molecules, has been shown to be elevated during EAE[32].

Quantification of the number of meningeal T cells during disease progression revealed an increased density of T cells inside and around the meningeal lymphatic vasculature, corresponding with the emergence of clinical symptoms (Supplementary Fig. 6g–i), implying an increase in meningeal immune cell egress in the draining lymph nodes. This suggests that, in contrast to peripheral lymphatics, meningeal lymphatics might not demonstrate a classical inflammation-induced lymphangiogenesis.

Meningeal vasculature is subordinate to an environment that might physically constrain the vessels; we therefore decided to further investigate the endogenous properties of the meningeal LECs as compared to those from the diaphragm and skin (ear). Cells were fluorescence-activated cell sorted from WT mice as previously described[1] and RNA-seq was performed. Principal component analysis showed a clustering of the samples in a tissue-specific manner (Fig. 4a). Differential expression analysis showed that ~300 genes were specifically up- or downregulated in the meningeal lymphatics compared to peripheral lymphatics (Fig. 4b, c), whereas LEC-specific gene set enrichment analysis revealed no difference between these three sources of cells (Fig. 4d). Gene set enrichment analysis showed alterations of multiple pathways related to extracellular matrix, focal adhesion, and angiogenesis, but also of pathways related to response to endogenous and exogenous stimuli (Fig. 4e). The meningeal LECs appear, then, to possess unique gene sets that enable their interaction with the meningeal environment. Of note, several molecules previously implicated in lymphatic development and proliferation[33–35] were dysregulated in the meningeal compared to peripheral lymphatics (Fig. 4f). Furthermore, the role of environmental stiffness has been demonstrated in regulation of the LEC transcriptome and response to growth factors[36]. When compared to peripheral lymphatics, expression of stiffness-regulated genes by meningeal LEC was similar to their expression by LECs cultured on a stiff matrix[36,37] (Fig. 4g). Such an expression profile may underlie the limited ability of adult meningeal LECs to respond to growth factors or local inflammation.

Ablation of meningeal lymphatic drainage ameliorated EAE pathology. Although meningeal lymphatics did not change morphologically during EAE-associated inflammation, we decided to assess their role in EAE. Previous reports, using different models of EAE, show a critical role of the dCLNs in disease severity[38–40]. We confirmed in our model that the resection of the dCLNs (Supplementary Fig. 7a) led to decreased disease severity. Using a Visudyne-based approach, we found that disruption of the meningeal lymphatics also delayed the development of EAE and resulted in milder disease pathology (Fig. 5a, b). Notably, ablation of the nasal lymphatics using Visudyne, while preventing drainage into the sCLNs (Fig. 3q), did not interfere with the disease development (Fig. 5a, b). Similar results were obtained via surgical ligation of the afferent lymphatics of the dCLNs (Supplementary Fig. 7b,c). In line with these findings, analysis of the CNS compartments during the active phase of EAE (day 17 postimmunization) revealed lower numbers of CD4 T cell infiltrates in the spinal cord parenchyma while the numbers of CD4 T cells remained higher in the brain meninges (Fig. 5c, d). Collectively, these results suggest that the dCLNs represent an important site for the induction or maintenance of encephalitogenic T cells and that drainage of the CSF into dCLNs might be key for the lymph node to harbor this unique characteristic.

Analysis of T cell activation and proliferation in the spleen and dCLNs of mice with normal and ablated lymphatic drainage was comparable (Supplementary Fig. 7d–h). To test the hypothesis that lymphatic drainage is necessary to shape T cell phenotypes, we analyzed the interactions of brain antigen-specific T cells (MOG, or 2D2) and nonbrain antigen-specific T cells (ovalbumin, or OTII) with dendritic cells ($CD11c^+$) in the dCLNs of EAE mice. For this purpose, adult C57Bl6 mice were seeded with a 1:1 ratio of fluorescent 2D2 and OTII T cells 1 d before meningeal lymphatic ablation and EAE induction. Proliferation of 2D2 T cells was not affected by the ablation of the meningeal lymphatics (Fig. 5e–h). Notably, we found that the interaction of 2D2 (but not OTII) T cells with $CD11c^+$ cells, quantified as a contact between two cells, was significantly reduced in mice with meningeal lymphatic ablation (Fig. 5f–h). This result suggests that the lack of lymphatic drainage reduced T cell–APC interactions. Quantification of APCs in dCLNs of control and ablated mice did not show differences (Supplementary Fig. 7i).

To better understand how CNS lymphatic drainage impacts T cell encephalitogenicity, we analyzed the transcriptomic profile of dCLN-isolated antigen-specific T cells. Adult mice were injected with naive fluorescent 2D2 (MOG-specific) T cells before meningeal lymphatic ablation and EAE induction, and cells were harvested from the spleen and dCLNs 8 d after EAE induction. We found that about 500 genes were significantly up- or downregulated in the 2D2 T cells activated in the dCLNs without lymphatic drainage when compared to control EAE mice (without lymphatic manipulation), with the majority of the genes being downregulated (Fig. 5i, j). Notably, no difference in gene expression was observed in the spleens of these mice (Fig. 5i). Gene ontology on unadjusted normalized gene counts revealed a significant downregulation of multiple pathways related to the inflammatory response and, more precisely, to cytokine and chemokine responses and production in T cells (Fig. 5k). Multiple downregulated genes (Fig. 5j) have been previously identified as promoting EAE development (*Ccr1*[41]), are involved in T cell activation and differentiation (*Tradd*[42]), or relate to migration and vascular transmigration (*Nod2*[43]). Furthermore, prediction of active miRNAs revealed a potentially increased activity of miRNA implicated in T cell activation, differentiation, and migration, such as miR Let7[44] (Fig. 5l). Overall, this transcriptomic analysis suggests that the lack of lymphatic drainage prevented the acquisition of the fully encephalitogenic profile by MOG-specific T cells in the dCLNs, in turn resulting in decreased migration and encephalitogenic properties of T cells into the CNS and milder clinical scores. These results suggest an active role for cellular and/or molecular drainage in modulating T cell phenotype in response to CNS antigens and highlight how lymphatic drainage regulates tissue-specific immune responses.

Discussion

Here we show that meningeal lymphatic vessels sample macromolecules and immune cells from the CSF and serve as an important conduit for CNS drainage. We also describe structural features of spinal cord meningeal lymphatics. We expand on our understanding of immune-cell trafficking via the meningeal lymphatic vessels to the draining lymph nodes, which is primarily dependent on CCR7. Using a pharmacological method that we adopted to specifically ablate meningeal (or nasal) lymphatic vessels, we demonstrated that the nasal route drains directly into the sCLNs, while the meningeal lymphatic route drains into both the dCLNs and sCLNs. RNA-seq analysis of LECs from mouse meninges, diaphragm, and skin revealed that the meningeal lymphatic vessels exhibited a unique transcriptional profile, which, under local inflammatory conditions, might underlie the distinct behavior of meningeal lymphatics. Attenuation of EAE was obtained after surgical and pharmacological blockade of lymphatic function, suggesting that drainage contributed to the activation of encephalitogenic T cells in the lymph nodes. Supporting this notion, reduction of meningeal lymphatic drainage

reduced interactions of 2D2 T cells with local antigen-presenting cells. RNA-seq of activated 2D2 T cells isolated from dCLNs showed that T cells from mice lacking lymphatic drainage acquired a different phenotype from that of controls. These findings warrant further research to identify the cellular (and/or molecular) mediators draining from the CNS and driving T cell encephalitogenicity.

Meningeal lymphatic vessels are embedded within the dura[11,12]. This raises an obvious question: how can macromolecules and immune cells drain from the CSF into meningeal lymphatic vessels, given that the arachnoid mater is supposedly impermeable to CSF[45]? We noticed, however, that certain spots along the meningeal lymphatics could be seen to take up the tracer from the CSF almost immediately after its injection, whereas tracer uptake along remaining parts of the vessels was slower. Subsequent experiments revealed certain spots along the meningeal lymphatics where the vessel structure was more complex and ramified and where extensions were exposed to the CSF. The structure of these lymphatic sprouts is reminiscent of peripheral-tissue lymphatic buttons[14], which serve as entry gates into the lymphatic vasculature[14]. Further experiments using electron microscopy technique will be necessary to demonstrate that the meningeal lymphatic vessels are physically crossing the arachnoid mater.

Previous reports have implicated the cribriform plate as a major player in the passage of immune cells from the CNS to its draining lymph nodes[9]. Furthermore, a recent study has challenged the potential contribution of the meningeal lymphatics in the drainage of CSF into the CLNs[6]. Here using live-imaging, our data (supported by others[46]) clearly demonstrates the uptake by meningeal lymphatics of tracers injected into the CSF. Our observations, however, do not exclude alternative routes as previously suggested.

In the present study, we injected exogenous cells into the cisterna magna and also observed cells in the nasal mucosa and associated lymphatics. However, we could not detect any T cells on the nasal side of the cribriform plate under physiological conditions. Moreover, we labeled endogenous meningeal T cells using laser photoconversion but could not detect any labeled cells in the nasal mucosa. It is possible that if photoconversion of meningeal T cells was complete, some crossing of the cribriform plate by meningeal T cells could have been observed. Furthermore, the speed of injection (and, hence, change in intracranial pressure) appears to be a major factor in facilitating crossing of the cribriform plate by CNS immune cells. Our results thus suggest that the cribriform plate in all probability does not represent a major physiological immune-relevant exit route. This structure has been shown, however, to play an important role in the regulation of CSF homeostasis, since its surgical blockade results in an immediate and constant increase in CSF pressure[47]. Our results also show that chronic neuroinflammation is accompanied by expansion of the lymphatic vasculature localized around the cribriform plate (as opposed to brain and spinal cord meningeal lymphatics), suggesting that the nasal region might have a more important function at later stages of disease development.

Several organs (such as lungs[48], for example) have been suggested as sites at which CNS-specific T cells become 'licensed' to acquire an appropriate migratory profile that will allow them to infiltrate the CNS. Our data suggest that dCLNs could be another site for T cell licensing or reactivation. Dendritic cells migrating from different tissues have been shown to uniquely influence T cell activation and migration[49], and MOG-loaded dendritic cells reportedly activate T cells in the CLNs before their migration into the CNS[50]. In the context of EAE (both induced and spontaneous), excision of the brain-draining lymph nodes has been shown to delay or attenuate disease development[38–40]. In spontaneous models, limitation of the drainage of MOG into the dCLNs, thereby preventing activation of MOG-specific T cells, is a likely mechanism. A similar scenario might apply when meningeal lymphatics are ablated. It is important to note that meningeal lymphatic ablation only attenuates and ameliorates EAE but does not completely stop it, suggesting that other routes are involved. Although no side effects were found when using the Visudyne approach, future development of targeted techniques will allow researchers to discern the role of anatomically distinct lymphatics in EAE.

Overall, the work described here provides the first characterization, to our knowledge, of the meningeal lymphatic system in the context of brain immunity and neuroinflammation and opens the way to a better understanding of brain immune surveillance and the generation of CNS-directed immune responses. These results might help to uncover the etiology of the immune imbalance typical of neuroinflammatory disorders, with promising implications for therapy.

Online content

Any methods, additional references, Nature Research reporting summaries, source data, statements of data availability and associated accession codes are available at https://doi.org/10.1038/s41593-018-0227-9.

Received: 19 April 2018; Accepted: 2 August 2018;
Published online: 17 September 2018

References

1. Louveau, A. et al. Structural and functional features of central nervous system lymphatic vessels. *Nature* **523**, 337–341 (2015).
2. Kida, S., Pantazis, A. & Weller, R. O. CSF drains directly from the subarachnoid space into nasal lymphatics in the rat. Anatomy, histology and immunological significance. *Neuropathol. Appl. Neurobiol.* **19**, 480–488 (1993).
3. Cserr, H. F., Harling-Berg, C. J. & Knopf, P. M. Drainage of brain extracellular fluid into blood and deep cervical lymph and its immunological significance. *Brain. Pathol.* **2**, 269–276 (1992).
4. Iliff, J. J. et al. A paravascular pathway facilitates CSF flow through the brain parenchyma and the clearance of interstitial solutes, including amyloid β. *Sci. Transl. Med.* **4**, 147ra111 (2012).
5. Go, K. G., Houthoff, H. J., Hartsuiker, J., Blaauw, E. H. & Havinga, P. Fluid secretion in arachnoid cysts as a clue to cerebrospinal fluid absorption at the arachnoid granulation. *J. Neurosurg.* **65**, 642–648 (1986).
6. Ma, Q., Ineichen, B. V., Detmar, M. & Proulx, S. T. Outflow of cerebrospinal fluid is predominantly through lymphatic vessels and is reduced in aged mice. *Nat. Commun.* **8**, 1434 (2017).
7. Kipnis, J. Multifaceted interactions between adaptive immunity and the central nervous system. *Science* **353**, 766–771 (2016).
8. Aspelund, A. et al. A dural lymphatic vascular system that drains brain interstitial fluid and macromolecules. *J. Exp. Med.* **212**, 991–999 (2015).
9. Engelhardt, B., Vajkoczy, P. & Weller, R. O. The movers and shapers in immune privilege of the CNS. *Nat. Immunol.* **18**, 123–131 (2017).
10. Louveau, A. et al. Understanding the functions and relationships of the glymphatic system and meningeal lymphatics. *J. Clin. Invest.* **127**, 3210–3219 (2017).
11. Andres, K. H., von Düring, M., Muszynski, K. & Schmidt, R. F. Nerve fibres and their terminals of the dura mater encephali of the rat. *Anat. Embryol. (Berl.)* **175**, 289–301 (1987).
12. Absinta, M. et al. Human and nonhuman primate meninges harbor lymphatic vessels that can be visualized noninvasively by MRI. *eLife* **6**, e29738 (2017).
13. Kamphorst, A. O., Guermonprez, P., Dudziak, D. & Nussenzweig, M. C. Route of antigen uptake differentially impacts presentation by dendritic cells and activated monocytes. *J. Immunol.* **185**, 3426–3435 (2010).
14. Baluk, P. et al. Functionally specialized junctions between endothelial cells of lymphatic vessels. *J. Exp. Med.* **204**, 2349–2362 (2007).
15. Castrén, E. & Antila, H. Neuronal plasticity and neurotrophic factors in drug responses. *Mol. Psychiatry* **22**, 1085–1095 (2017).
16. Földi, M. et al. New contributions to the anatomical connections of the brain and the lymphatic system. *Acta Anat.* **64**, 498–505 (1966).
17. Antila, S. et al. Development and plasticity of meningeal lymphatic vessels. *J. Exp. Med.* **214**, 3645–3667 (2017).
18. Hennet, T., Hagen, F. K., Tabak, L. A. & Marth, J. D. T-cell-specific deletion of a polypeptide N-acetylgalactosaminyl-transferase gene by site-directed recombination. *Proc. Natl. Acad. Sci. USA* **92**, 12070–12074 (1995).
19. Derecki, N. C. et al. Regulation of learning and memory by meningeal immunity: a key role for IL-4. *J. Exp. Med.* **207**, 1067–1080 (2010).
20. Ziarek, J. J. et al. Structural basis for chemokine recognition by a G protein-coupled receptor and implications for receptor activation. *Sci. Signal.* **10**, eaah5756 (2017).

21. Debes, G. F. et al. Chemokine receptor CCR7 required for T lymphocyte exit from peripheral tissues. *Nat. Immunol.* **6**, 889–894 (2005).
22. Weber, M. et al. Interstitial dendritic cell guidance by haptotactic chemokine gradients. *Science* **339**, 328–332 (2013).
23. Randolph, G. J., Ivanov, S., Zinselmeyer, B. H. & Scallan, J. P. The lymphatic system: integral roles in immunity. *Annu. Rev. Immunol.* **35**, 31–52 (2017).
24. Clarkson, B. D. et al. CCR7 deficient inflammatory dendritic cells are retained in the central nervous system. *Sci. Rep.* **7**, 42856 (2017).
25. Wigle, J. T. & Oliver, G. Prox1 function is required for the development of the murine lymphatic system. *Cell* **98**, 769–778 (1999).
26. Harvey, N. L. et al. Lymphatic vascular defects promoted by *Prox1* haploinsufficiency cause adult-onset obesity. *Nat. Genet.* **37**, 1072–1081 (2005).
27. Lavado, A. & Oliver, G. Prox1 expression patterns in the developing and adult murine brain. *Dev. Dyn.* **236**, 518–524 (2007).
28. Tammela, T. et al. Photodynamic ablation of lymphatic vessels and intralymphatic cancer cells prevents metastasis. *Sci. Transl. Med.* **3**, 69ra11 (2011).
29. Kim, H., Kataru, R. P. & Koh, G. Y. Inflammation-associated lymphangiogenesis: a double-edged sword? *J. Clin. Invest.* **124**, 936–942 (2014).
30. Dendrou, C. A., Fugger, L. & Friese, M. A. Immunopathology of multiple sclerosis. *Nat. Rev. Immunol.* **15**, 545–558 (2015).
31. Ajami, B. et al. Single-cell mass cytometry reveals distinct populations of brain myeloid cells in mouse neuroinflammation and neurodegeneration models. *Nat. Neurosci.* **21**, 541–551 (2018).
32. Proescholdt, M. A., Jacobson, S., Tresser, N., Oldfield, E. H. & Merrill, M. J. Vascular endothelial growth factor is expressed in multiple sclerosis plaques and can induce inflammatory lesions in experimental allergic encephalomyelitis rats. *J. Neuropathol. Exp. Neurol.* **61**, 914–925 (2002).
33. Cursiefen, C. et al. Thrombospondin 1 inhibits inflammatory lymphangiogenesis by CD36 ligation on monocytes. *J. Exp. Med.* **208**, 1083–1092 (2011).
34. Jurisic, G. et al. An unexpected role of semaphorin3a-neuropilin-1 signaling in lymphatic vessel maturation and valve formation. *Circ. Res.* **111**, 426–436 (2012).
35. Mäkinen, T. et al. PDZ interaction site in ephrinB2 is required for the remodeling of lymphatic vasculature. *Genes Dev.* **19**, 397–410 (2005).
36. Frye, M. et al. Matrix stiffness controls lymphatic vessel formation through regulation of a GATA2-dependent transcriptional program. *Nat. Commun.* **9**, 1511 (2018).
37. Yeh, Y. T. et al. Matrix stiffness regulates endothelial cell proliferation through septin 9. *PLoS One* **7**, e46889 (2012).
38. Furtado, G. C. et al. Swift entry of myelin-specific T lymphocytes into the central nervous system in spontaneous autoimmune encephalomyelitis. *J. Immunol.* **181**, 4648–4655 (2008).
39. Phillips, M. J., Needham, M. & Weller, R. O. Role of cervical lymph nodes in autoimmune encephalomyelitis in the Lewis rat. *J. Pathol.* **182**, 457–464 (1997).
40. van Zwam, M. et al. Surgical excision of CNS-draining lymph nodes reduces relapse severity in chronic-relapsing experimental autoimmune encephalomyelitis. *J. Pathol.* **217**, 543–551 (2009).
41. Rottman, J. B. et al. Leukocyte recruitment during onset of experimental allergic encephalomyelitis is CCR1 dependent. *Eur. J. Immunol.* **30**, 2372–2377 (2000).
42. Guan, Y. J. et al. Phospho-SXXE/D motif mediated TNF receptor 1-TRADD death domain complex formation for T cell activation and migration. *J. Immunol.* **187**, 1289–1297 (2011).
43. Wu, X., Lahiri, A., Haines, G. K. III, Flavell, R. A. & Abraham, C. NOD2 regulates CXCR3-dependent CD8+T cell accumulation in intestinal tissues with acute injury. *J. Immunol.* **192**, 3409–3418 (2014).
44. Jeker, L. T. & Bluestone, J. A. MicroRNA regulation of T-cell differentiation and function. *Immunol. Rev.* **253**, 65–81 (2013).
45. Brinker, T., Stopa, E., Morrison, J. & Klinge, P. A new look at cerebrospinal fluid circulation. *Fluids Barriers CNS* **11**, 10 (2014).
46. Cai, R. et al. Panoptic vDISCO imaging reveals neuronal connectivity, remote trauma effects and meningeal vessels in intact transparent mice. Preprint at *bioRxiv* https://doi.org/10.1101/374785 (2018).
47. Mollanji, R., Bozanovic-Sosic, R., Zakharov, A., Makarian, L. & Johnston, M. G. Blocking cerebrospinal fluid absorption through the cribriform plate increases resting intracranial pressure. *Am. J. Physiol. Regul. Integr. Comp. Physiol.* **282**, R1593–R1599 (2002).
48. Odoardi, F. et al. T cells become licensed in the lung to enter the central nervous system. *Nature* **488**, 675–679 (2012).
49. Mora, J. R. et al. Reciprocal and dynamic control of CD8 T cell homing by dendritic cells from skin- and gut-associated lymphoid tissues. *J. Exp. Med.* **201**, 303–316 (2005).
50. Zozulya, A. L. et al. Intracerebral dendritic cells critically modulate encephalitogenic versus regulatory immune responses in the CNS. *J. Neurosci.* **29**, 140–152 (2009).

Acknowledgements

We thank S. Smith for editing the manuscript. We also thank all the members of the Kipnis lab and the members of the Center for Brain Immunology and Glia (BIG) for their valuable comments during multiple discussions of this work. This work was supported by grants from the National Institutes of Health (AG034113 and NS096967), National Multiple Sclerosis Society (NMSS), and the German Research Council (DFG; CRC-TR-128, B11) to J.K.; National Institutes of Health HL073402 to G.O.; Howard Hughes Medical Institute Medical Research Fellow Program to M.Q.D. and by Henry M. Weitzner, Edna K. Weitzner, Dorothea M. Weitzner, Morton L. Weitzner and Lymphatic Education & Research Network postdoctoral fellowship to A.L.

Author contributions

A.L. designed and performed most of the experiments and wrote the manuscript; J.H. designed and performed the experiments related to the spinal cord lymphatics and CCR7-dependent cellular migration; M.N.A. initiated experiments related to cribriform plate and nasal lymphatics; A.F.S. assisted A.L. with experimental procedures and analysis; M.Q.D. assisted J.H. with spinal cord lymphatic related experiments; K.E.V. assisted A.L. with experimental procedures; G.H. assisted A.L. with experimental procedures; J. Knopp assisted A.L. with experimental procedures; J.S. assisted A.L. with experimental procedures; A.L.L. assisted J.H. with experimental procedures; S.D.M. helped with experimental procedures; E.L.F. performed the multiplex experiment on CSF; I.S. performed ligation surgeries, intracranial pressure measurements, and harvested CSF; R.C. performed the experiments related to photoacoustic microscopy; S.H. designed the experiments related to photoacoustic microscopy; A.G. helped with initial EAE induction and scoring; T.H.H. contributed intellectually to experimental design through multiple discussions; J.R.L. designed the multiplex experiment; C.C.O. provided bioinfomatic analysis of the data; G.O. provided $Prox1^{het}$ mice and helped with experiments design related to these mice and writing; J. Kipnis designed experiments, supervised the work, and wrote the manuscript.

Competing interests

J. Kipnis is an Advisor to PureTech Health/Ariya.

Additional information

Supplementary information is available for this paper at https://doi.org/10.1038/s41593-018-0227-9.

Correspondence and requests for materials should be addressed to A.L. or J.K.

Methods

Mice. Mice were maintained and bred in-house under standard housing conditions (12-h light/dark cycles and fed ad libitum). All mice were on a C57Bl/6J background except for the Prox1^{LacZ} (identified as Prox1^{het} in the manuscript), which were on an NMRI background. Both adult males and females were used unless stated otherwise, at 8–12 weeks of age. Only female mice were used for the immunization experiments. Strains used are C57Bl/6J (JAX: 000664); Prox1^{LacZ} (gift from G. Oliver, Northwestern University, Feinberg School of Medecine, Chicago, IL, USA); B6.129P2(C)-Ccr7$^{TM1RFOR/J}$ (CCR7KO; JAX: 006621); C57Bl/6-Ccr7$^{tm1.1Dnc}$/J (CCR7GFP; JAX: 027913); Tg(CAG-KiKGR)33Hadj/J (KiKGR; JAX: 013753); Prox1^{GFP}/Prox1^{tdTOMATO} (gift from Y.K. Hong, Division of Plastic and Reconstructive Surgery, Department of Surgery, Keck School of Medicine, University of South California, Los Angeles, CA, USA); Prox1^{CreERT2} (gift from T. Makinen, Department of Immunology, Genetics and Pathology, Uppsala University, Uppsala, Sweden); Gt(ROSA)26Sor$^{tm1(DTA)}$Lky/J (ROSA DTA; JAX: 009669); Gt(ROSA)26Sor$^{tm1(HBEGF)Awai}$/J (ROSA DTR; JAX: 007900); C57Bl/6-Tg(Tcra2D2, Tcrb2D2)1Kuch/J (2D2; JAX: 006912); B6.Cg-Tg(TcraTcrb)425Cbn/J (OTII; JAX: 004194); B6.Cg-Tg$^{(Lck\text{-}cre)548Jxm}$/J (Lck-Cre; JAX: 0038802); B6.129P-Cx3cr1tmLitt/J (CX3CR1^{GFP}; JAX: 005582); and Gt(ROSA)26Sor$^{tm14(CAG\text{-}tdTOMATO)Hze}$/J (ROSA tdTOMATO; JAX: 007914). Experimenters were blinded to experimental groups during scoring and quantifications. Sample sizes were chosen in accordance with similar previously published experiments. Animals from different cages in the same experimental group were selected to assure randomization. All experiments were approved by the Institutional Animal Care and Use Committee of the University of Virginia.

Intracisterna magna (i.c.m.) injection. Mice were anesthetized with ketamine/xylazine i.p. and injected i.c.m. into the cisterna magna. We then injected 2 µL of fluorescent beads mix (0.75 µL FluoSpheres Carboxylate-Modified Microspheres of 1.0-µm diameter (ThermoFisher) plus 0.5 µL FluoSpheres Carboxylate-Modified Microspheres 0.5-µm diameter (ThermoFisher) in a total volume of 2 µL PBS), 5 µL of FluoSpheres Carboxylate-Modified Microsphere of 0.5 µm, or 5 µL of Alexa Fluor 594/647-conjugated OVA (0.5mg/ml; ThermoFisher) at a rate of 0.5 µL/min (unless indicated otherwise). After injection, the needle was left in place for 1–2 min to avoid backflow. Subsequently, the muscle was pinched to apply some pressure on the cisterna magna before needle removal. Mice were then sutured and allowed to recover on a heating pad until responsive (after about 45 min to 1 h). Lymph nodes and meninges were harvested at the indicated timepoints and analyzed by immunohistochemistry or flow cytometry.

Vasculature labeling. Mice were injected i.v. with 50 µL of DyLight 488-labeled *Lycopersicon esculentum* (DL-1174; Vector Laboratories) 2–3 min before the mouse was killed for analysis.

Stereotactic injections. Mice were anesthetized with ketamine/xylazine i.p. and immobilized on a stereotactic frame. Intracerebroventricular (i.c.v.) injections were performed for the right lateral ventricle at 1 mm lateral, –0.6 mm longitudinal from bregma, and the needle lowered –2 mm. Then 0.5 µL of FluoSpheres Carboxylate-Modified Microspheres of 0.5-µm size (ThermoFisher) were reconstituted in 2 µL PBS and delivered at the indicated rate of injection with a syringe pump. The skin was sutured and mice treated with analgesic.

Lymph nodes excision and surgical ligation. Mice were anesthetized with ketamine/xylazine (i.p.), shaved at the neck (or armpit), cleaned with iodine and 70% ethanol, and an ophthalmic solution was put on the eyes to prevent drying. For dCLN resection or ligation, an incision was made along the midline, 5 mm superior to the clavicle. The sternocleidomastoid muscle (SCN) was retracted, and the dCLN were removed with forceps. For ligation, the collecting lymphatic vessels anterior to the dCLN were ligated using a nylon suture (11–0, nylon nonabsorbable monofilament suture, AD Surgical). For the brachial lymph nodes, an incision was made at the bottom of the triceps. The brachial lymph nodes were either resected using forceps or had their collecting lymphatic ligated using a nylon suture (11–0, nylon nonabsorbable monofilament suture, AD Surgical). Mice were then sutured and allowed to recover on a heating pad until responsive. Postsurgery, mice were given analgesic and antibiotics subcutaneously.

Visudyne treatment. Visudyne treatment protocol was adapted from previous publications[28,51,52]. Mice were anesthetized with ketamine/xylazine (i.p.). Visudyne (Valeant Ophtalmics) was reconstituted following manufacturer instructions and either 5 µL was injected i.c.m. into the cisterna magna (for meningeal lymphatic ablation) or 2 µL was injected in each nostril (for nasal lymphatics ablation). After 15 min, Visudyne was photoconverted with a nonthermal 689-nm wavelength laser light (Coherent Opal Photoactivator, Lumenis) on 5 different spots through the intact skull (1 on the cisterna magna, 2 on the transverse sinuses, 1 on the superior sagittal sinus, and 1 at the junction of all sinuses). For nasal lymphatic ablation, the laser was applied through the soft palate of the mouse's mouth. Each spot was irradiated with a light dose of 50 J/cm^2 at an intensity of 600 mW/cm^2 for 83 s. Mice were then sutured and allowed to recover on a heating pad until responsive. Postsurgery, mice were given analgesic subcutaneously.

Experimental autoimmune encephalomyelitis. EAE was induced in female mice by subcutaneous injection of MOG_{35-55} peptide (200 µg, CSBio) emulsified in Freund's adjuvant (Sigma Aldrich) supplemented with 2 mg/mL of *Mycobacterium tuberculosis* (BD). Pertussis toxin (200 ng, List Biologicals) was injected i.p. on day 0 and day 1 after MOG immunization. For clinical evaluation, mice were scored daily: 0 = no clinical disease, 1 = limp tail, 2 = hindlimb weakness, 3 = hindlimb paralysis, 4 = partial front limb paralysis, 5 = moribund.

Intracranial pressure measurement. Mice were anesthetized (ketamine/xylazine, i.p.) and the skin was incised to expose the skull. A 0.5-mm diameter hole was drilled in the skull above the right parietal lobe. A pressure sensor (model SPR100; Millar) was inserted perpendicularly into the cortex at a depth of 1 mm. The pressure sensor was connected to a PCU-2000 pressure control unit (Millar) and recorded for 5 min after stabilization of the signal (around a minute after insertion of the probe). The average pressure was calculated over the last 2 min of recording (between minutes 4 and 6 of the recording). Animals were killed at the conclusion of the measurement. For positive control, adult C57Bl6 mice were submitted to bilateral ligation of the jugular vein[53,54]. For negative control, adult C57Bl6 were injected intraperitoneally with 20 mg/kg of acetazolamide (Sigma) dissolved in DMSO (Sigma)[55].

Photoacoustic imaging. Adult mice were anesthetized with 1.5% isoflurane and body temperature was maintained with the aid of a temperature controlled heating pad. A surgical incision was made in the scalp and the fascia was removed to expose the skull. The skull over the region of interest was thinned to the desired thickness (100 µm) one day before the imaging. Mice were then imaged by multiparametric photoacoustic microscopy (PAM), which is capable of simultaneously image oxygen saturation of hemoglobin (sO_2) and blood flow speed as described previously[56]. sO2 is computed from the oxyhemoglobin (HbO_2) and deoxyhemoglobin (Hbr) recorded using two nanosecond-pulsed lasers (532 and 559 nm). Correlation analysis of adjacent A-line signals allows the quantification of blood flow speed within individual vessels. By segmenting major vessels within the region of interest, average values of the sO_2 and blood flow speed were extracted for quantitative analysis.

Multiphoton microscopy. Adult Prox1^{GFP},Lck^{Cre}::tdTOMATO$^{loxP/loxP}$ mice were anesthetized by ketamine/xylazine intraperitoneal (i.p.) injection. Mice were injected intravenously (i.v.) or into the cisterna magna (i.c.m.) with Qtracker655 vascular tracker (ThermoFisher; Qdot^{655}, 5 µL with 95 µL saline (i.v.) or 5 µL (i.c.m.)). Furamidine dihydrochloride (125 µg, Sigma Aldrich) was injected i.v. before imaging. Meningeal lymphatic vessels were imaged through a thinned skull preparation above the superior sagittal, transverse sinuses, or cerebellum. The core temperature of the mice was maintained at 37 °C. Imaging was performed with a Leica TCS SP8 multiphoton system (Leica Microsystems) equipped with a Chameleon Ultra II tunable Ti:sapphire laser (Coherent). GFP, tdTOMATO, and Qdot^{655} were excited with an excitation wavelength of 880 nm (or 780 nm for furamidine[57]). Second harmonic signals (bone and meningeal signals) were visualized using a 400/450 external detector. Images were obtained using a 25× water immersion objective with 0/95 NA and external HyD non-descanned detectors (Leica Microsystems). Three-dimensional image data were collected by obtaining images from the *x*, *y* and *z* planes. The resulting images were analyzed with Imaris software (Bitplane).

Photoconversion of KiKGR. Mice were anesthetized with 3% isoflurane (vol/vol). Incision of the skin above the skull was performed to expose the skull from in between the eyes to the lower part of the cerebellum. Aluminum foil was used to cover the mouse except the skull to ensure local conversion. Photoconversion was performed using an Optogenetics-LED-Violet module (Prizmatix) for 2 min at an intensity of 6 with the light source placed 1 cm above the skull. Mice were then sutured and allowed to recover on a heating pad until responsive. Postsurgery, mice were given analgesic subcutaneously. For DC migration experiments, skull bone of anesthetized mice was exposed to violet light for 3 min per spot in 3 locations: 2 spots above the transverse sinus and 1 spot in the center of the superior sagittal sinus. Immediately after illumination, Kikume green fluorescent (KiKG$^+$) meningeal cells become red fluorescent (KiKR$^+$)[58]. Repeated conversion led to a photoconversion efficiency of 70–92% of CD45 cells in the meninges (with differential effect depending on the population, as indicated in the text). Soluble peptide (10 µg GP_{33-42}/KAVYNFATC) and 2 µg of poly(I:C) were injected i.c.m. to mobilize local DCs.

Diphtheria toxin and tamoxifen injection. Prox1^{CreERT2}::DTR$^{loxP/loxP}$ mice and Prox1^{CreERT2} were injected i.c.m. with 250 ng, 25 ng. 2.5 ng, or 0.25 ng of diphtheria toxin (Calbiochem). Injections were repeated 4 and 7 d after the initial injection. Mice weight and survival were followed for 10 d. Meninges of surviving mice were analyzed by immunohistochemistry. Prox1^{CreERT2}::DTA$^{loxP/loxP}$ mice and Prox1^{CreERT2} were injected i.c.m. with 0.1 mg/µL of 4-hydroxitamoxifen (one injection, 4 µL total, Sigma Aldrich) or 100 µg, 20 µg, or 10 µg of 4-hydroxitamoxifen (3 injection every 3 d, 4 µL total, Sigma Aldrich). Mice weight and survival were followed for 10 d. Meninges of surviving mice were analyzed by immunohistochemistry.

Generation of dendritic cells and labeling. DCs were generated from flushed femurs and tibiae bone marrow suspension as previously described[55,59]. At day 8 of culture with GM-CSF (20 ng/mL recombinant protein; eBioscience), DCs were matured overnight with lipopolysaccharide (200 ng/mL LPB-EB Ultrapure; Invivogen). Wild-type or CCR7-KO DCs were differently labeled with 5 µM CFSE (eBioscience) or 10 µM TAMRA (Molecular Probes) in serum-free RPMI medium for 20 min at room temperature (20–25 °C) and washed twice with complete RPMI, then resuspended at a concentration of 2.5×10^5 cells/µL for i.c.m. injection (2 µL total).

T cells isolation and labeling. Mice were killed for analysis with an i.p. injection of Euthasol. Spleen and lymph nodes (inguinal, brachial, axillary, cervical, mesenteric, and lumbar) were harvested and gently pressed through a 70-µm nylon mesh cell strainers (Fisher) with sterile plastic plunger (BD Biosciences) to yield a single-cell suspension. Red blood cells were lysed by 5 min incubation in ACK lysis buffer (Quality Biologicals). T cells were then enriched using the EasySep Mouse CD4 T cells isolation kit (STEMCELL Technologies) following the manufacturer's instructions.

To generate activated memory T cells, purified CD4 T cells were plated at 1×10^6 cells/mL in a petri dish previously coated with 2 µg/mL of anti-CD3 (clone 17A2, BioXCell) and anti-CD28 (clone PV-1, BioXCell) O/N. After 48 h, cells were transferred into a new petri dish with 50% fresh media (RPMI (Gibco) with 10% FBS (Atlas Biologicals), 1% penicillin/streptomycin (Gibco), 1% L-glutamine (Gibco), and 50 µM β-mercaptoethanol (Gibco)) supplemented with 100 U/mL of rIL-2 (eBioscience). IL-2 supplementation was repeated every other day until day 9. Cells were split in half and supplemented with fresh media on day 5.

Prior to injection, T cells were labeled with CFSE (eBioscience), CellTracker Deep Red Dye (ThermoFisher), or CellTrace Violet (ThermoFisher) following the manufacturer's instructions. T cells (1 million total in 2 µL) were injected i.c.m. into anesthetized mice (ketamine/xylazine, i.p.) using a Hamilton syringe with a 33-gauge needle.

Pertussis toxin treatment. As previously described[60], isolated T cells were incubated for 2 h at 37 °C with 200 ng/mL of PTX (List Biological) in media (RPMI (Gibco) with 10% FBS (Atlas Biologicals), 1% penicillin/streptomycin (Gibco), 1% L-glutamine (Gibco), and 50 µM β-mercaptoethanol (Gibco)). Cells were then washed 3 times with media and labeled before injection.

Tissue collection and processing. Mice were killed for analysis by i.p. injection of Euthasol and perfused with 0.1 M of PBS (10–15 mL/mouse).

- Lymph nodes were harvested using forceps and placed in PBS with 4% paraformaldehyde (PFA) overnight for immunohistochemistry. For flow cytometry, LNs were either digested with collagenase D (1 mg/mL; Roche) and DNAse (50 U/mL; Sigma) for 30 min at 37 °C or kept in ice-cold FACS buffer (pH 7.4; 0.1 M PBS; 1 mM EDTA; 1% BSA) before mechanical dissociation using a piston and 70-µm nylon filter mesh (Fisher Scientific). dCLNs were harvested from the side of the internal jugular vein while sCLNs were harvested from the upper part of the salivary gland. For IHC, lymph nodes were transferred in PBS containing 30% sucrose O/N at 4 °C. Lymph nodes were then embedded in OCT and 30-µm-thick sections were sliced onto gelatin-coated slides on a cryostat (Leica).
- Skin was then removed from the head and the muscles were stripped off the bone. After removal of the mandibles, the nose was sectioned (below the olfactory bulbs) with a scalpel and placed in PBS with 4% PFA for 72 h. The nose was decalcified by incubation in PBS with 0.1 M of EDTA for 6 d (with daily changes of the decalcification solution) and transferred in PBS with 30% sucrose O/N. Noses were then embedded in OCT and 50-µm-thick sections (coronal or sagittal) were sliced onto gelatin-coated slides on a cryostat (Leica).
- Brains were placed in 4% paraformaldehyde (PFA) solution for 3 d, transferred in PBS with 30% sucrose O/N, embedded in OCT, and 40-µm-thick section (coronal) were sliced on a cryostat (Leica).
- Whole-mount meninges were fixed, while still attached to the skullcap, in PBS with 2% PFA for 24 h at 4 °C (for IHC) or dissected and transferred in ice-cold FACS buffer for flow cytometry. Meninges (dura/arachnoid) were then dissected from the skullcap.
- Spinal columns were fixed in PBS with 4% PFA for 2 d at 4 °C. The bone on the ventral side of the vertebrae was cut laterally and taken off to expose the spinal cord. Nervous tissue was dissected with fine forceps, and meninges cut along the ventral site and peeled from the spinal cord as a whole.

Immunohistochemistry. Whole-mounts and sections were incubated with PBS containing 2% of normal serum (either goat or chicken), 1% BSA, anti-CD16/32 (eBioscience, 1:1,000) 0.1% Triton X-100, and 0.05% Tween 20 for 1 h at room temperature (RT), followed by incubation with appropriate dilutions (1:200) of primary antibodies O/N at 4C in PBS containing 1% BSA and 0.5% Triton X-100. Primary antibodies used were: anti-alpha smooth muscle actin (C6198; Sigma Aldrich); goat polyclonal anti-CCL21 (AF457; R&D Systems); rat anti-CD3e (12-0032-81; BD Biosciences); armenian hamster anti-CD31 (MAB1398.Z; Millipore); mouse anti-claudin-5 AF488-conjugated (352588; ThermoFisher); rabbit anti-GFAP (Z0334; Dako); goat anti-Iba1(ab5076; Abcam); rabbit anti-laminin1 & 2 (ab7463; Abcam); rat anti-Lyve-1 biotinylated (13-0443-82; eBioscience); rat anti-Lyve-1 AF488-conjugated (53-0443-82; eBioscience); rat anti-Lyve-1 eF660-conjugated (50-0443-82, eBioscience); Syrian hamster anti-podoplanin biotinylated (12-5381-82; eBioscience); goat anti-VEGFR3 (AF743; R&D Systems); rat anti-VE-cadherin (CD144) biotinylated (13-1441-80; eBioscience); and chicken polyclonal anti-beta3-tubulin (Ab9354; Chemicon). Whole-mounts and sections were washed 3 times for 5 min at RT with PBS followed by incubation with Alexa Fluor 488/594/647 chicken/goat antibodies (Invitrogen, 1:1,000), Alexa Fluor 594/647 goat anti-Armenian hamster IgG antibodies (Jackson ImmunoResearch, 1:1,000), or BV480-conjugated streptavidin (BD Biosciences, 1:500) for 1 h at RT in PBS with 1% BSA and 0.5% Triton X-100. After 5 min in 1:20,000 DAPI reagent (Sigma-Aldrich), whole-mounts and sections were washed with PBS and mounted with Aqua-Mount (Lerner) under coverslips.

Image analysis. Images were acquired with a Leica TCS SP8 confocal system (Leica Microsystems) using LSA AF software. Images were acquired with a 10× objective with 0.25 NA or 20× objective with 0.70 NA, with a resolution of 512×512 or 1,024×1,024 pixels with a *z*-step of 4 µm. Quantitative assessments were performed using FIJI software (NIH) or Imaris software (Bitplane). Density of injected T cells or dendritic cells was determined by dividing the number of labeled T cells/DCs per section by the area of the lymph node section. Bead coverage was quantified by dividing the area occupied by the beads over the area of the lymph nodes. Every other section, covering the totality of the lymph nodes, was quantified (~15–20 sections per lymph node). Lymphatic ablation was measured either by dividing the area occupied by Lyve-1 immunostaining by the area of the sinus or by dividing the total length of lymphatics by the total length of the sinuses. Macrophages size was determined by averaging the $Iba1^+$ area of 10 individual cells randomly chosen per animal.

Statistical analyses were performed using GraphPad Prism software. Specific statistical tests are presented in the text for each experiment. Outlier samples were eliminated using Grubbs' test with a significance level of 0.05. No estimate of variation between groups was performed.

Flow cytometry. Mice were killed for analysis by perfusion with 0.1 M PBS (10–15 mL). Meninges, lymph nodes, spleen, and spinal cord were then dissected. Lymph nodes and spleen were either digested with collagenase D (1 mg/mL; Roche) and DNAse I (50 U/mL) or gently pressed through 70-µm nylon mesh cell strainers with a sterile plastic plunger (BD Biosciences) to yield a single-cell suspension. Spinal cords were stripped of their meninges before digestion for 45 min in 4 U/mL of papain (Worthington Biochemical) and 50 U/mL of DNAse I (Sigma Aldrich) at 37 °C before being strained. Cells were then centrifuged at 300*g* at 25 °C for 10 min. Spinal cord cells were resuspended in 37% Percoll (Fisher) and centrifuged at 1,200*g* for 30 min without braking. Meninges were digested for 15 min at 37 °C with 1.4 U/mL of Collagenase VIII (Sigma Aldrich) and 35 U/mL of DNAse I (Sigma Aldrich) in complete media (DMEM (Gibco) with 2% FBS (Atlas Biologicals), 1% L-glutamine (Gibco), 1% penicillin/streptomycin (Gibco), 1% sodium pyruvate (Gibco), 1% nonessential amino acid (Gibco), and 1.5% HEPES (Gibco)). The cell pellets (for all tissues) were resuspended in ice-cold FACS buffer (pH 7.4; 0.1 M PBS; 1 mM EDTA, and 1% BSA). Cells were stained for extracellular markers with the following antibodies at a 1:200 dilution: rat monoclonal anti-B220 PE-conjugated (553090; BD Biosciences); rat anti-CCR7 APC-conjugated (17-1971-63; BioLegend); rat anti-CD4 APC-conjugated (553051; BD Biosciences); rat anti-CD4 PerCP-Cy5.5-conjugated (550954; BD Biosciences); rat anti-CD8 Pacific Blue-conjugated (558106; BD Biosciences); rat anti-CD11b PE-conjugated (12-0112-82; eBioscience); Armenian hamster anti-CD11c PE-conjugated (12-0114-82; eBioscience); Armenian hamster anti-CD11c BV421-conjugated (562782; BD Bioscience); Armenian hamster anti-CD11c APC-conjugated (17-0114-82; eBioscience); rat anti-CD19 AF700-conjugated (557958; BD Biosciences); rat anti-CD40 APC-conjugated (17-0401-81; eBioscience); rat anti-CD44 APC-conjugated (559250; BD Biosciences); rat anti-CD45 biotin-conjugated (553078; BD Biosciences); rat anti-CD45 BV510-conjugated (563891; BD Biosciences); rat anti-CD45 PerCP-Cy5.5-conjugated (550994; BD Biosciences); mouse anti-CD45.2 AF700-conjugated (109822; BioLegend); hamster anti-CD54 PE-conjugated (553253; BD Biosciences); rat anti-CD62L PE-CF594-conjugated (562404; BD Biosciences); rat anti-CD62L PE-conjugated (12-0621-83; eBioscience); Armenian hamster anti-CD69 PE-Cy7-conjugated (552879; BD Biosciences); Armenian hamster CD80 APC-conjugated (17-0801-81; eBioscience); Armenian hamster anti-CD103 APC-conjugated (17-1031-82; eBioscience); rat anti-CD106 FITC-conjugated (11-1061-81; ThermoFisher); rat anti-FoxP3 eFluor450-conjugated (48-5773-82; eBioscience); anti-ICAM PE-conjugated (12-0549-42; ThermoFisher) rat anti-IFNγ FITC-conjugated (554411; BD Biosciences); rat anti-IL-17 PerCP-Cy5.5-conjugated (45-7177-82; eBioscience); rat anti-IL-17A AF700-conjugated (560820; BD Biosciences); rat anti-Ly6C PerCP-Cy5.5-conjugated (560525; BD Biosciences); rat anti-Ly6G AF700-conjugated (561236; BD Biosciences); rat anti-I-A/I-E PE-conjugated (12-5321-82; eBioscience); rat anti-I-A/I-E PE-Cy7-conjugated (25-5321-82; eBioscience); mouse anti-NK1.1 PE-Cy7-conjugated (552878; BD Biosciences); rat anti-Siglec-F BV421-conjugated (562681; BD Biosciences); Armenian

hamster anti-TCRb APC-Cy7-conjugated (557656; BD Biosciences); Armenian hamster anti-TCRb FITC-conjugated (11-5961-85; eBioscience); Armenian hamster anti-TCRb BV711-conjugated (563613; BD Biosciences); Armenian hamster anti-TCRb BV510-conjugated (563221; BD Biosciences); rat anti-Thy1.2 FITC-conjugated (553013; BD Biosciences), and Armenian hamster anti-TCRb PE-conjugated (12-5961-81; eBioscience).. Cells were then fixed in 1% PFA in 0.1 M pH 7.4 PBS. For intracellular staining, cells were fixed and permeabilized following the manufacturer's instructions (BD Biosciences), then incubated with antibodies directed toward intracellular markers diluted in Perm/Wash buffer (BD Biosciences). Fluorescence data were collected with a Gallios (Beckman Coulter), then analyzed using FlowJo software (Treestar). Single cells were gated using the height, area, and pulse-width of the forward and side scatter, then cells were selected for being live cells using the LIVE/DEAD Fixable Dead Cell Strain Kit per the manufacturer's instructions (Invitrogen). Cells were then gated for the appropriate marker of cell type. An aliquot of unstained cells was counted using Cellometer Auto2000 (Nexcelor) to provide an accurate cell count from the samples. Data processing was done with Excel and statistical analysis performed using GraphPad Prism.

T cell activation and proliferation. Splenocytes were collected from mice at D8 of EAE development. Cells were labeled with CellTrace Violet (ThermoFisher) following the manufacturer's instructions and plated at 500,000 cells/200 µL with CD3/CD28 (2 µg/mL each, BioXCell) or increasing concentration of MOG_{35-55} (CSbio) for 72 h. Data were acquired on a Gallios (Beckman Coulter) and analyzed with FlowJo software (Treestar). Splenocytes and dCLN were collected from mice at D8 of EAE development and stimulated for 6 h with 20 ng/mL PMA (eBioscience), 1 µg/mL ionomycin (eBioscience), and 10 µg/mL brefeldin A (Sigma Aldrich). Cells were then washed and immunostained.

Cell sorting and RNA-seq analysis. To FACS sort lymphatic endothelial cells (LEC), meninges, skin (ear), and diaphragm were collected after the mice were killed for analysis and systemically perfused with PBS. Skin and diaphragm were physically minced before digestion. Tissues were incubated for 15 min at 37 °C with 1.4 U/mL of Collagenase VIII (Sigma Aldrich) and 35 U/mL of DNAse I (Sigma Aldrich) in complete media (DMEM (Gibco) with 2% FBS (Atlas Biologicals), 1% L-glutamine (Gibco), 1% penicillin/streptomycin (Gibco), 1% sodium pyruvate (Gibco), 1% nonessential amino acid (Gibco) and 1.5% HEPES (Gibco)). Tissues were then pelleted after filtration through a 70-µm nylon mesh cell strainer and immunostained as described before. To FACS sort T cells, spleen and lymph nodes were harvested after the mice were killed for analysis and systemically perfused with PBS. A single-cell suspension was obtained by gentle pressing on a 70-µm nylon mesh cell strainer. Cells were then immunostained as previously described. Cells were sorted in a 96-well plate in 100 µL of lysis buffer (Arcturus PicoPure RNA Isolation Kit) using the Influx Cell Sorter (BD Biosciences).

RNA was isolated from FACS sorted cells using the Arcturus PicoPure RNA Isolation Kit. For RNA sequencing, all postprocessing (including linear RNA amplification and cDNA library generation) and sequencing was performed by Hudson Alpha Genomic Services Laboratory.

The raw sequencing reads (FASTQ files) went through two stages of processing to remove low-quality reads and bases as previously published[61]. First, they were chastity filtered, which removes any clusters that have a higher-than-expected intensity of the called base compared to other bases. Then they were trimmed with Trimmomatic to remove low-quality bases (minimum read length after trimming = 36). After processing, the quality of the reads was evaluated using FastQC, and after passing quality control (QC), they were aligned to the UCSC mm9 genome using the splice-aware read-aligner STAR. The quality of the alignments was next assessed by SAMStat, and low-quality alignments were removed with samtools (MAPQ < 10). Next, the number of reads aligning to each gene was quantified with HTSeq and then with the Bioconductor package. DESeq2 was used to normalize the raw counts and to perform exploratory analysis (for example, PCA) and differential expression analysis. The Benjamini–Hochberg false discovery rate procedure was used to correct *P* values for multiple testing. Heatmaps of the differentially expressed genes generated with the R package heatmap and the T implementation of Fisher's exact test (fisher.test) was used to identify enriched gene sets in the differentially expressed gens using the gene set collections from MSigDB (C5) and the gene families from the Hugo Gene Nomenclature Committer (HGNC).

Multiplex immunoassay. CSF was collected from the cisterna magna (see "Intracisterna magna injection" for animal preparation) under a dissection microscope using a glass capillary (Sutter Instrument, B100-50-10, pulled with a Sutter Instrument P-30 micropipette puller to a size of 0.5 mm in diameter). We pooled 10 µl of the obtained volume from two mice and used it for quantifying cytokines using Luminex magnetic beads following the Bio-Plex Pro Mouse Chemokine Panel 33-plex instruction (Bio-Rad). Data were acquired with a Bio-Plex 200 with HTF and analyzed with the Bio-Plex Manager software Version 6.1.

Statistical analysis. Sample sizes were chosen on the basis of standard power calculations (with $\alpha = 0.05$ and power of 0.8) performed for similar experiments. In general, statistical methods were not used to recalculate or predetermine sample sizes. The Kolmogorov–Smirnov test was used to assess normal distribution of the data, or data distribution was assumed to be normal but this was not formally tested. Variance was similar within comparable experimental groups. Animals from different cages, but within the same experimental group, were selected to assure randomization. Experimenters were blinded to the identity of experimental groups from the time mice were killed for analysis until the end of data collection and analysis for at least one of the independent experiments. Statistical tests for each figure were justified to be appropriate. One-way ANOVA with appropriate multiple-comparison tests were used to compare three independent groups. Two-group comparisons were made using two-tailed unpaired Student's *t* test. For comparisons of multiple factors, two-way ANOVA with appropriate multiple-comparisons tests were used. Repeated-measures two-way ANOVA with appropriate multiple-comparisons tests were used for clinical symptom evaluations with repeated observations. Statistical analysis (data are always presented as mean ± s.e.m.) was performed using Prism 6.0a (GraphPad Software, Inc.).

Reporting Summary. Further information on research design is available in the Nature Research Reporting Summary linked to this article.

Data availability

All RNA-seq datasets are available at GEO: LEC experiment, GSE99743; T cell lymphatic ablation experiment, GSE99764. The data that supports the finding of the study are available from the corresponding authors upon reasonable request.

References

51. Kilarski, W. W. et al. Optimization and regeneration kinetics of lymphatic-specific photodynamic therapy in the mouse dermis. *Angiogenesis* **17**, 347–357 (2014).
52. Wachowska, M. et al. Investigation of cell death mechanisms in human lymphatic endothelial cells undergoing photodynamic therapy. *Photodiagnosis Photodyn. Ther.* **14**, 57–65 (2016).
53. Ensari, S. et al. Venous outflow of the brain after bilateral complete jugular ligation. *Turk. Neurosurg.* **18**, 56–60 (2008).
54. Kawajiri, H., Furuse, M., Namba, R., Kotani, J. & Oka, T. Effect of internal jugular vein ligation on resorption of cerebrospinal fluid. *J. Maxillofac. Surg.* **11**, 42–45 (1983).
55. Vogh, B. P., Godman, D. R. & Maren, T. H. Effect of AlCl3 and other acids on cerebrospinal fluid production: a correction. *J. Pharmacol. Exp. Ther.* **243**, 35–39 (1987).
56. Ning, B. et al. Ultrasound-aided multi-parametric photoacoustic microscopy of the mouse brain. *Sci. Rep.* **5**, 18775 (2015).
57. Coles, J. A. et al. Intravital imaging of a massive lymphocyte response in the cortical dura of mice after peripheral infection by trypanosomes. *PLoS Negl. Trop. Dis.* **9**, e0003714 (2015).
58. Nowotschin, S. & Hadjantonakis, A. K. Use of KikGR a photoconvertible green-to-red fluorescent protein for cell labeling and lineage analysis in ES cells and mouse embryos. *BMC Dev. Biol.* **9**, 49 (2009).
59. Oshio, K., Watanabe, H., Song, Y., Verkman, A. S. & Manley, G. T. Reduced cerebrospinal fluid production and intracranial pressure in mice lacking choroid plexus water channel Aquaporin-1. *FASEB J.* **19**, 76–78 (2005).
60. Cyster, J. G. & Goodnow, C. C. Pertussis toxin inhibits migration of B and T lymphocytes into splenic white pulp cords. *J. Exp. Med.* **182**, 581–586 (1995).
61. Da Mesquita, S. et al. Functional aspects of meningeal lymphatics in ageing and Alzheimer's disease. *Nature* **560**, 185–191 (2018).

nature research

Corresponding author(s): Jonathan Kipnis

Reporting Summary

Nature Research wishes to improve the reproducibility of the work that we publish. This form provides structure for consistency and transparency in reporting. For further information on Nature Research policies, see Authors & Referees and the Editorial Policy Checklist.

Statistical parameters

When statistical analyses are reported, confirm that the following items are present in the relevant location (e.g. figure legend, table legend, main text, or Methods section).

n/a	Confirmed	
☐	☒	The exact sample size (*n*) for each experimental group/condition, given as a discrete number and unit of measurement
☐	☒	An indication of whether measurements were taken from distinct samples or whether the same sample was measured repeatedly
☐	☒	The statistical test(s) used AND whether they are one- or two-sided *Only common tests should be described solely by name; describe more complex techniques in the Methods section.*
☐	☒	A description of all covariates tested
☐	☒	A description of any assumptions or corrections, such as tests of normality and adjustment for multiple comparisons
☐	☒	A full description of the statistics including central tendency (e.g. means) or other basic estimates (e.g. regression coefficient) AND variation (e.g. standard deviation) or associated estimates of uncertainty (e.g. confidence intervals)
☐	☒	For null hypothesis testing, the test statistic (e.g. *F*, *t*, *r*) with confidence intervals, effect sizes, degrees of freedom and *P* value noted *Give P values as exact values whenever suitable.*
☒	☐	For Bayesian analysis, information on the choice of priors and Markov chain Monte Carlo settings
☒	☐	For hierarchical and complex designs, identification of the appropriate level for tests and full reporting of outcomes
☒	☐	Estimates of effect sizes (e.g. Cohen's *d*, Pearson's *r*), indicating how they were calculated
☐	☒	Clearly defined error bars *State explicitly what error bars represent (e.g. SD, SE, CI)*

Our web collection on statistics for biologists may be useful.

Software and code

Policy information about availability of computer code

Data collection	The following software were used for data collection: - Bio-Plex 200 with HTF (BioRad) - Kaluza Acquisition Software for Gallios (Beckman Coulter) - LAS X Software (Leica)
Data analysis	The following software were used for data analysis: - FIJI image processing software (NIH) - v2.0.0-rc-59/1.51n - FlowJo version (v) 10 (TreeStar) - Imaris v8.1 (Bitplane) - GraphPad Prism v6 (GraphPad Softwarem Inc) - Bio-Plex Manager Software v6.1 (BioRad) - OsiriX v9.0 - FastQC v0.11.5 - Salmon v0.8.2 - R v3.4.2 - Bioconductor DESeq2 v3.5 - Excel 14.7.7 - Trimmomatic v0.36 (USADELLAB)

- STAR
- SAMStat v1.5

For manuscripts utilizing custom algorithms or software that are central to the research but not yet described in published literature, software must be made available to editors/reviewers upon request. We strongly encourage code deposition in a community repository (e.g. GitHub). See the Nature Research guidelines for submitting code & software for further information.

Data

Policy information about availability of data

All manuscripts must include a data availability statement. This statement should provide the following information, where applicable:

- Accession codes, unique identifiers, or web links for publicly available datasets
- A list of figures that have associated raw data
- A description of any restrictions on data availability

All RNA-seq data sets are available online (GEO database) under the accession numbers: LEC experiment is GSE99743 and the T cell lymphatic ablation experiment is GSE99764. This statement is included in the manuscript, page 56. The files with all the raw data will be provided (through Mendeley or an alternative platform) once the manuscript is accepted. We could immediately provide the link to our data for the reviewers/editors.

Field-specific reporting

Please select the best fit for your research. If you are not sure, read the appropriate sections before making your selection.

☒ Life sciences ☐ Behavioural & social sciences

For a reference copy of the document with all sections, see nature.com/authors/policies/ReportingSummary-flat.pdf

Life sciences

Study design

All studies must disclose on these points even when the disclosure is negative.

Sample size	Sample size was chosen in accordance with similar previously published experiments.
Data exclusions	Outlier samples were eliminated using Grubbs' test with a significance level of 0.05
Replication	Experiments were performed by using several mice of each genotype or condition. The whole experiment was repeated several times or performed in such a way that independent data were obtained and statistical significance testing applied. Findings that were not replicated were validated by additional experimental methodology (e.g. dural leakage was determined by intra-vital imaging and immunohistochemistry on independent sets of mice).
Randomization	Animals from different cages in the same experimental group were selected to assure randomization
Blinding	Experimental groups were blinded during scoring and quantifications

Materials & experimental systems

Policy information about availability of materials

n/a	Involved in the study
☒	☐ Unique materials
☐	☒ Antibodies
☒	☐ Eukaryotic cell lines
☐	☒ Research animals
☒	☐ Human research participants

Antibodies

Antibodies used	In vitro: Anti-CD3 (clone 17A2, BioXCell); Anti-CD28 (clone PV-1, BioXCell) Immunohistochemistry: Anti-alpha smooth muscle actin (C6198; Sigma Aldrich); Goat polyclonal anti-CCL21 (AF457; R&D Systems); Rat anti-CD3e (12-0032-81; BD Biosciences); Armenian hamster anti-CD31 (MAB1398.Z; Millipore); Mouse anti-Claudin-5 AF488 conjugated (352588; ThermoFisher); Rabbit anti-GFAP (Z0334; Dako); Goat anti-Iba1 (ab5076; Abcam); Rabbit anti-Laminin1&2 (ab7463; Abcam); Rat anti-Lyve-1 biotinylated (13-0443-82; eBioscience); Rat anti-Lyve-1 AF488 conjugated (53-0443-82; eBioscience); Rat anti-Lyve-1 eF660 conjugated (50-0443-82, eBioscience); Syrian hamster anti-podoplanin biotinylated (12-5381-82; eBioscience); Goat anti-VEGFR3 (AF743; R&D Systems); Rat anti-VE-cadherin (CD144) biotinylated (13-1441-80; eBioscience); Chicken polyclonal anti-beta3-tubulin (Ab9354; Chemicon); Alexa-fluor 488/594/647 chicken/goat

antibodies (Invitrogen, 1:1000), Alexa-fluor 594/647 goat anti-Armenian Hamster IgG antibodies (Jackson ImmunoResearch, 1:1000)
Flow Cytometry: Rat monoclonal anti-B220 PE conjugated (553090; BD Biosciences); Rat anti-CCR7 APC conjugated (17-1971-63; Biolegend); Rat anti-CD4 APC conjugated (553051; BD Biosciences); Rat anti-CD4 PerCP-Cy5.5 conjugated (550954; BD Biosciences); Rat anti-CD8 Pacific blue conjugated (558106; BD Biosciences); Rat anti-CD11b PE conjugated (12-0112-82; eBioscience); Armenian hamster anti-CD11c PE conjugated (12-0114-82; eBioscience); Armenian hamster anti-CD11c BV421 conjugated (562782; BD Bioscience); Armenian hamster anti-CD11c APC conjugated (17-0114-82; eBioscience); Rat anti-CD19 AF700 conjugated (557958; BD Biosciences); Rat anti-CD40 APC conjugated (17-0401-81; eBioscience); Rat anti-CD44 APC conjugated (559250; BD Biosciences); Rat anti-CD45 Biotin conjugated (553078; BD Biosciences); Rat anti-CD45 BV510 conjugated (563891; BD Biosciences); Rat anti-CD45 PerCP Cy5.5 conjugated (550994; BD Biosciences); Mouse anti-CD45.2 AF700 conjugated (109822; Biolegend); Hamster anti-CD54 PE conjugated (553253; BD Biosciences); Rat anti-CD62L PE-CF594 conjugated (562404; BD Biosciences); Rat anti-CD62L PE conjugated (12-0621-83; eBioscience); Armenian hamster anti-CD69 PE-Cy7 conjugated (552879; BD Biosciences); Armenian hamster CD80 APC conjugated (17-0801-81; eBioscience); Armenian hamster anti-CD103 APC conjugated (17-1031-82; eBioscience); Rat anti-CD106 FITC conjugated (11-1061-81; ThermoFisher); Rat anti-FoxP3 eFluor450 conjugated (48-5773-82; eBioscience); Anti-ICAM PE conjugated (12-0549-42; ThermoFisher) Rat anti-IFNg FITC conjugated (554411; BD Biosciences); Rat anti-IL-17 PerCP-Cy5.5 conjugated (45-7177-82; eBioscience); Rat anti-IL-17A AF700 conjugated (560820; BD Biosciences); Rat anti-Ly6C PerCP-Cy5.5 conjugated (560525; BD Biosciences); Rat anti-Ly6G AF700 conjugated (561236; BD Biosciences); Rat anti-I-A/I-E PE conjugated (12-5321-82; eBioscience); Rat anti-I-A/I-E PE-Cy7 conjugated (25-5321-82; eBioscience); Mouse anti-NK1.1 PE-Cy7 conjugated (552878; BD Biosciences); Rat anti-Siglec-F BV421 conjugated (562681; BD Biosciences); Armenian hamster anti-TCRb APC-Cy7 conjugated (557656; BD Biosciences); Armenian hamster anti-TCRb FITC conjugated (11-5961-85; eBioscience); Armenian hamster anti-TCRb BV711 conjugated (563613; BD Biosciences); Armenian hamster anti-TCRb BV510 conjugated (563221; BD Biosciences); Rat anti-Thy1.2 FITC conjugated (553013 – BD Biosciences); Armenian hamster anti-TCRb PE conjugated (12-5961-81; eBioscience).

Validation

Each antibody was validated for the species (mouse) and application (immunohistochemistry or flow cytometry/cell sorting) by the correspondent manufacturer. The usage was described in the methods section of the manuscript:
Immunohistochemistry: Whole mount and section were incubated with PBS containing 2% of normal serum (either goat or chicken), 1% BSA, anti-CD16/32 (eBioscience, 1:1000) 0.1% Triton-X-100 and 0.05% Tween 20 for 1h at room temperature (RT), followed by incubation with appropriate dilutions (1:200) of primary antibodies O/N at 4C in PBS containing 1% BSA and 0.5% Triton-X-100. Primary antibodies used were: Anti-alpha smooth muscle actin (C6198; Sigma Aldrich); Goat polyclonal anti-CCL21 (AF457; R&D Systems); Rat anti-CD3e (12-0032-81; BD Biosciences); Armenian hamster anti-CD31 (MAB1398.Z; Millipore); Mouse anti-Claudin-5 AF488 conjugated (352588; ThermoFisher); Rabbit anti-GFAP (Z0334; Dako); Goat anti-Iba1(ab5076; Abcam); Rabbit anti-Laminin1&2 (ab7463; Abcam); Rat anti-Lyve-1 biotinylated (13-0443-82; eBioscience); Rat anti-Lyve-1 AF488 conjugated (53-0443-82; eBioscience); Rat anti-Lyve-1 eF660 conjugated (50-0443-82, eBioscience); Syrian hamster anti-podoplanin biotinylated (12-5381-82; eBioscience); Goat anti-VEGFR3 (AF743; R&D Systems); Rat anti-VE-cadherin (CD144) biotinylated (13-1441-80; eBioscience); and Chicken polyclonal anti-beta3-tubulin (Ab9354; Chemicon). Whole mounts and sections were washed 3 times for 5 min RT with PBS followed by incubation with Alexa-fluor 488/594/647 chicken/goat antibodies (Invitrogen, 1:1000), Alexa-fluor 594/647 goat anti-Armenian Hamster IgG antibodies (Jackson ImmunoResearch, 1:1000) or BV480 conjugated streptavidin (BD Biosciences, 1:500) for 1h at RT in PBS with 1% BSA and 0.5% Triton-X-100. After 5 min in 1:20 000 DAPI reagent (Sigma-Aldrich), whole mount and sections were washed with PBS and mounted with Aqua-Mount (Lerner) under coverslips.
Flow Cytometry: Mice were perfused with 0.1M PBS (10-15ml). Meninges, lymph nodes, spleen and spinal cord were then dissected. Lymph nodes and spleen were either digested with collagenase D (1 mg/ml; Roche) and DNAse I (50U/ml) or gently pressed through 70µm nylon mesh cell strainers with sterile plastic plunger (BD Biosciences) to yield a single cell suspension. For spinal cord, they were stripped of their meninges prior to digestion for 45min in 4U/ml of papain (Worthington Biochemical) and 50U/ml of DNAse I (Sigma Aldrich) at 37C prior to being strained. Cells were then centrifuged at 300g at 25°C for 10 min. Spinal cord cells were resuspended in 37% Percoll (Fisher) and centrifuged at 1200g for 30 min without brake. Meninges were digested 15min at 37C with 1.4U/ml of Collagenase VIII (Sigma Aldrich) and 35U/ml of DNAse I (Sigma Aldrich) in complete media (DMEM (Gibco) with 2% FBS (Atlas Biologicals), 1% L-Glutamine (Gibco), 1% penicillin/streptomycin (Gibco), 1% Sodium pyruvate (Gibco), 1% non-essential amino-acid (Gibco) and 1.5% Hepes (Gibco)). The cell pellets (for all tissues) were resuspended in ice-cold FACS buffer (pH7.4; 0.1M PBS; 1mM EDTA and 1% BSA). Cells were stained for extracellular marker with the following antibodies: Rat monoclonal anti-B220 PE conjugated (553090; BD Biosciences); Rat anti-CCR7 APC conjugated (17-1971-63; Biolegend); Rat anti-CD4 APC conjugated (553051; BD Biosciences); Rat anti-CD4 PerCP-Cy5.5 conjugated (550954; BD Biosciences); Rat anti-CD8 Pacific blue conjugated (558106; BD Biosciences); Rat anti-CD11b PE conjugated (12-0112-82; eBioscience); Armenian hamster anti-CD11c PE conjugated (12-0114-82; eBioscience); Armenian hamster anti-CD11c BV421 conjugated (562782; BD Bioscience); Armenian hamster anti-CD11c APC conjugated (17-0114-82; eBioscience); Rat anti-CD19 AF700 conjugated (557958; BD Biosciences); Rat anti-CD40 APC conjugated (17-0401-81; eBioscience); Rat anti-CD44 APC conjugated (559250; BD Biosciences); Rat anti-CD45 Biotin conjugated (553078; BD Biosciences); Rat anti-CD45 BV510 conjugated (563891; BD Biosciences); Rat anti-CD45 PerCP Cy5.5 conjugated (550994; BD Biosciences); Mouse anti-CD45.2 AF700 conjugated (109822; Biolegend); Hamster anti-CD54 PE conjugated (553253; BD Biosciences); Rat anti-CD62L PE-CF594 conjugated (562404; BD Biosciences); Rat anti-CD62L PE conjugated (12-0621-83; eBioscience); Armenian hamster anti-CD69 PE-Cy7 conjugated (552879; BD Biosciences); Armenian hamster CD80 APC conjugated (17-0801-81; eBioscience); Armenian hamster anti-CD103 APC conjugated (17-1031-82; eBioscience); Rat anti-CD106 FITC conjugated (11-1061-81; ThermoFisher); Rat anti-FoxP3 eFluor450 conjugated (48-5773-82; eBioscience); Anti-ICAM PE conjugated (12-0549-42; ThermoFisher) Rat anti-IFNγ FITC conjugated (554411; BD Biosciences); Rat anti-IL-17 PerCP-Cy5.5 conjugated (45-7177-82; eBioscience); Rat anti-IL-17A AF700 conjugated (560820; BD Biosciences); Rat anti-Ly6C PerCP-Cy5.5 conjugated (560525; BD Biosciences); Rat anti-Ly6G AF700 conjugated (561236; BD Biosciences); Rat anti-I-A/I-E PE conjugated (12-5321-82; eBioscience); Rat anti-I-A/I-E PE-Cy7 conjugated (25-5321-82; eBioscience); Mouse anti-NK1.1 PE-Cy7 conjugated (552878; BD Biosciences); Rat anti-Siglec-F BV421 conjugated (562681; BD Biosciences); Armenian hamster anti-TCRb APC-Cy7 conjugated (557656; BD Biosciences); Armenian hamster anti-TCRb FITC conjugated (11-5961-85; eBioscience); Armenian hamster anti-TCRb BV711 conjugated (563613; BD Biosciences); Armenian hamster anti-TCRb BV510 conjugated (563221; BD Biosciences); Rat anti-Thy1.2 FITC conjugated (553013 – BD Biosciences) and Armenian hamster anti-TCRb PE conjugated (12-5961-81; eBioscience).. Cells were then fixed in 1% PFA in 0.1M pH7.4 PBS. For intracellular staining, cells where fixed and permeabilized following manufacturers instruction (BD Biosciences) then incubated with antibodies directed towards intracellular markers diluted in Perm/Wash buffer (BD Biosciences). Fluorescence data were

collected with a Gallios (Beckman Coulter) then analyzed using FlowJo software (Treestar). Single cells were gated using the height, area and the pulse width of the forward and side scatter, then cells were selected for being live cells using the LIVE/DEAD Fixable Dead Cell Strain Kit per the manufacturer's instructions (Invitrogen). Cells were then gated for the appropriate marker of cell type. An aliquot of unstained cells was counted using Cellometer Auto2000 (Nexcelor) to provide accurate cell count from the samples. Data processing was done with Excel and statistical analysis performed using GraphPad Prism.

Research animals

Policy information about studies involving animals; ARRIVE guidelines recommended for reporting animal research

Animals/animal-derived materials	All mice were on a C57Bl/6J background except for the Prox1LacZ (identified as Prox1Het in the manuscript) that were on an NMRI background. Both males and females were used unless stated otherwise. Only female mice were used for the immunization experiments. Strains used are C57Bl/6J (JAX: 000664); Prox1LacZ (gift from Guillermo Oliver); B6.129P2(C)-Ccr7TM1RFOR/J (CCR7KO – JAX: 006621); C57Bl/6-Ccr7tm1.1Dnc/J (CCR7GFP – JAX: 027913); Tg(CAG-KiKGR)33Hadj/J (KiKGR – JAX: 013753); Prox1GFP / Prox1tdTOMATO (gift from Dr. Young Kwon Hong); Prox1CreERT2. (gift from Dr. Taija Makinen); Gt(ROSA)26Sortm1(DTA)Lky/J (ROSA DTA – JAX: 009669); Gt(ROSA)26Sortm1(HBEGF)Awai/J (ROSA DTR – JAX: 007900); C57Bl/6-Tg(Tcra2D2, Tcrb2D2)1Kuch/J (2D2 – JAX: 006912); B6.Cg-Tg(TcraTcrb)425Cbn/J (OTII – JAX: 004194); B6.Cg-Tg(Lck-cre)548Jxm/J (Lck-Cre – JAX: 0038802); B6.129P-Cx3cr1tmLitt/J (CX3CR1GFP – JAX: 005582) and Gt(ROSA)26Sortm14(CAG-tdTOMATO)Hze/J (ROSA tdTOMATO – JAX: 007914). Mice were between 8 and 12 weeks of age.

Method-specific reporting

n/a	Involved in the study
☒	☐ ChIP-seq
☐	☒ Flow cytometry
☒	☐ Magnetic resonance imaging

Flow Cytometry

Plots

Confirm that:

☒ The axis labels state the marker and fluorochrome used (e.g. CD4-FITC).

☒ The axis scales are clearly visible. Include numbers along axes only for bottom left plot of group (a 'group' is an analysis of identical markers).

☒ All plots are contour plots with outliers or pseudocolor plots.

☒ A numerical value for number of cells or percentage (with statistics) is provided.

Methodology

Sample preparation	Mice were perfused with 0.1M PBS (10-15ml). Meninges, lymph nodes, spleen and spinal cord were then dissected. Lymph nodes and spleen were either digested with collagenase D (1 mg/ml; Roche) and DNAse I (50U/ml) or gently pressed through 70µm nylon mesh cell strainers with sterile plastic plunger (BD Biosciences) to yield a single cell suspension. For spinal cord, they were stripped of their meninges prior to digestion for 45min in 4U/ml of papain (Worthington Biochemical) and 50U/ml of DNAse I (Sigma Aldrich) at 37C prior to being strained. Cells were then centrifuged at 300g at 25°C for 10 min. Spinal cord cells were resuspended in 37% Percoll (Fisher) and centrifuged at 1200g for 30 min without brake. Meninges were digested 15min at 37C with 1.4U/ml of Collagenase VIII (Sigma Aldrich) and 35U/ml of DNAse I (Sigma Aldrich) in complete media (DMEM (Gibco) with 2% FBS (Atlas Biologicals), 1% L-Glutamine (Gibco), 1% penicillin/streptomycin (Gibco), 1% Sodium pyruvate (Gibco), 1% non-essential amino-acid (Gibco) and 1.5% Hepes (Gibco)). The cell pellets (for all tissues) were resuspended in ice-cold FACS buffer (pH7.4; 0.1M PBS; 1mM EDTA and 1% BSA). Cells were stained for extracellular marker with the following antibodies at a 1:200 dilution: Rat monoclonal anti-B220 PE conjugated (553090; BD Biosciences); Rat anti-CCR7 APC conjugated (17-1971-63; Biolegend); Rat anti-CD4 APC conjugated (553051; BD Biosciences); Rat anti-CD4 PerCP-Cy5.5 conjugated (550954; BD Biosciences); Rat anti-CD8 Pacific blue conjugated (558106; BD Biosciences); Rat anti-CD11b PE conjugated (12-0112-82; eBioscience); Armenian hamster anti-CD11c PE conjugated (12-0114-82; eBioscience); Armenian hamster anti-CD11c BV421 conjugated (562782; BD Bioscience); Armenian hamster anti-CD11c APC conjugated (17-0114-82; eBioscience); Rat anti-CD19 AF700 conjugated (557958; BD Biosciences); Rat anti-CD40 APC conjugated (17-0401-81; eBioscience); Rat anti-CD44 APC conjugated (559250; BD Biosciences); Rat anti-CD45 Biotin conjugated (553078; BD Biosciences); Rat anti-CD45 BV510 conjugated (563891; BD Biosciences); Rat anti-CD45 PerCP Cy5.5 conjugated (550994; BD Biosciences); Mouse anti-CD45.2 AF700 conjugated (109822; Biolegend); Hamster anti-CD54 PE conjugated (553253; BD Biosciences); Rat anti-CD62L PE-CF594 conjugated (562404; BD Biosciences); Rat anti-CD62L PE conjugated (12-0621-83; eBioscience); Armenian hamster anti-CD69 PE-Cy7 conjugated (552879; BD Biosciences); Armenian hamster CD80 APC conjugated (17-0801-81; eBioscience); Armenian hamster anti-CD103 APC conjugated (17-1031-82; eBioscience); Rat anti-CD106 FITC conjugated (11-1061-81; ThermoFisher); Rat anti-FoxP3 eFluor450 conjugated (48-5773-82; eBioscience); Anti-ICAM PE conjugated (12-0549-42; ThermoFisher) Rat anti-IFNγ FITC conjugated (554411; BD Biosciences); Rat anti-IL-17 PerCP-Cy5.5 conjugated (45-7177-82; eBioscience); Rat anti-IL-17A AF700 conjugated (560820; BD Biosciences); Rat anti-Ly6C PerCP-Cy5.5 conjugated (560525; BD Biosciences); Rat anti-Ly6G AF700 conjugated (561236; BD Biosciences); Rat anti-I-A/I-E PE conjugated (12-5321-82; eBioscience); Rat anti-I-A/I-E PE-Cy7 conjugated (25-5321-82; eBioscience); Mouse anti-NK1.1 PE-Cy7 conjugated (552878; BD Biosciences); Rat anti-Siglec-F BV421 conjugated (562681; BD Biosciences); Armenian hamster anti-TCRb APC-Cy7 conjugated (557656; BD Biosciences); Armenian hamster anti-TCRb FITC conjugated (11-5961-85; eBioscience); Armenian hamster anti-TCRb BV711 conjugated (563613; BD Biosciences); Armenian hamster anti-TCRb BV510 conjugated (563221; BD Biosciences); Rat anti-Thy1.2 FITC conjugated (553013

– BD Biosciences) and Armenian hamster anti-TCRb PE conjugated (12-5961-81; eBioscience).. Cells were then fixed in 1% PFA in 0.1M pH7.4 PBS. For intracellular staining, cells where fixed and permeabilized following manufacturers instruction (BD Biosciences) then incubated with antibodies directed towards intracellular markers diluted in Perm/Wash buffer (BD Biosciences). Fluorescence data were collected with a Gallios (Beckman Coulter) then analyzed using FlowJo software (Treestar). Single cells were gated using the height, area and the pulse width of the forward and side scatter, then cells were selected for being live cells using the LIVE/DEAD Fixable Dead Cell Strain Kit per the manufacturer's instructions (Invitrogen). Cells were then gated for the appropriate marker of cell type. An aliquot of unstained cells was counted using Cellometer Auto2000 (Nexcelor) to provide accurate cell count from the samples. Data processing was done with Excel and statistical analysis performed using GraphPad Prism.

Instrument	Acquisition was performed using Kaluza Acquisition software for Gallios.
Software	Analysis was performed using FlowJo V10 (TreeStar)
Cell population abundance	Purity was not assessed
Gating strategy	For all experiment, cells were gated on ==> single cells, live cells followed by the staining of interest. The gating strategy is indicated above each FACS plot in the figures.

☒ Tick this box to confirm that a figure exemplifying the gating strategy is provided in the Supplementary Information.